

Euclid preparation

Galaxy power spectrum modelling in redshift space

Euclid Collaboration: B. Camacho Quevedo^{1,2,3,4,5}, M. Crocce^{3,4}, M. Pellejero Ibañez⁶, R. E. Angulo^{7,8}, A. Pezzotta⁹, A. Eggemeier¹⁰, G. Gambardella^{3,4}, C. Moretti^{5,1,11}, E. Sefusatti^{5,1,11}, A. Moradinezhad Dizgah¹², M. Zennaro¹³, M.-A. Breton¹⁴, A. Chudaykin¹⁵, G. D'Amico^{16,17}, V. Desjacques¹⁸, S. de la Torre¹⁹, M. Guidi^{20,21}, M. Kärcher²², K. Pardede¹⁷, C. Porciani¹⁰, A. Pugno¹⁰, J. Salvalaggio^{5,1,23,11}, E. Sarpa^{2,24,5}, A. Veropalumbo^{9,25,26}, B. Altieri²⁷, S. Andreon⁹, N. Auricchio²¹, C. Baccigalupi^{1,5,11,2}, M. Baldi^{20,21,28}, S. Bardelli²¹, R. Bender^{29,30}, A. Biviano^{5,1}, E. Branchini^{26,25,9}, M. Brescia^{31,32}, S. Camera^{33,34,35}, V. Capobianco³⁵, C. Carbone³⁶, V. F. Cardone^{37,38}, J. Carretero^{39,40}, S. Casas^{41,42}, F. J. Castander^{3,4}, M. Castellano³⁷, G. Castignani²¹, S. Cavuoti^{32,43}, K. C. Chambers⁴⁴, A. Cimatti⁴⁵, C. Colodro-Conde⁴⁶, G. Congedo⁶, L. Conversi^{47,27}, Y. Copin⁴⁸, F. Courbin^{49,50,4}, H. M. Courtois⁵¹, H. Degaudenzi⁵², G. De Lucia⁵, H. Dole⁵³, M. Douspis⁵³, F. Dubath⁵², C. A. J. Duncan⁶, X. Dupac²⁷, S. Dusini⁵⁴, S. Escoffier⁵⁵, M. Farina⁵⁶, R. Farinelli²¹, S. Farrens¹⁴, S. Ferriol⁴⁸, F. Finelli^{21,57}, S. Fotopoulou⁵⁸, N. Fourmanoit⁵⁵, M. Frailis⁵, E. Franceschi²¹, M. Fumana³⁶, S. Galeotta⁵, K. George⁵⁹, B. Gillis⁶, C. Giocoli^{21,28}, J. Gracia-Carpio²⁹, A. Grazian⁶⁰, F. Grupp^{29,30}, L. Guzzo^{22,9,61}, S. V. H. Haugan⁶², W. Holmes⁶³, F. Hormuth⁶⁴, A. Hornstrup^{65,66}, K. Jahnke⁶⁷, B. Joachimi⁶⁸, S. Kermiche⁵⁵, A. Kiessling⁶³, B. Kubik⁴⁸, M. Kümmel³⁰, M. Kunz¹⁵, H. Kurki-Suonio^{69,70}, A. M. C. Le Brun⁷¹, S. Ligori³⁵, P. B. Lilje⁶², V. Lindholm^{69,70}, I. Lloro⁷², G. Mainetti⁷³, E. Maiorano²¹, O. Mansutti⁵, S. Marcin⁷⁴, O. Marggraf¹⁰, M. Martinelli^{37,38}, N. Martinet¹⁹, F. Marulli^{75,21,28}, R. J. Massey⁷⁶, E. Medinaceli²¹, M. Melchior⁷⁷, M. Meneghetti^{21,28}, E. Merlin³⁷, G. Meylan⁷⁸, A. Mora⁷⁹, M. Moresco^{75,21,28}, L. Moscardini^{75,21,28}, C. Neissner^{80,40}, S.-M. Niemi⁸¹, C. Padilla⁸⁰, S. Paltani⁵², F. Pasian⁵, K. Pedersen⁸², W. J. Percival^{83,84,85}, V. Pettorino⁸¹, S. Pires¹⁴, G. Polenta⁸⁶, M. Poncet⁸⁷, L. A. Popa⁸⁸, F. Raison²⁹, J. Rhodes⁶³, G. Riccio³², F. Rizzo⁵, E. Romelli⁵, M. Roncarelli²¹, R. Saglia^{30,29}, Z. Sakr^{89,90,91}, A. G. Sánchez²⁹, D. Sapone⁹², B. Sartoris^{30,5}, P. Schneider¹⁰, A. Secroun⁵⁵, G. Seidel⁶⁷, E. Sihvola⁹³, P. Simon¹⁰, C. Sirignano^{94,54}, G. Sirri²⁸, A. Spurio Mancini⁹⁵, L. Stanco⁵⁴, P. Tallada-Crespi^{39,40}, D. Tavagnacco⁵, A. N. Taylor⁶, I. Tereno^{96,97}, N. Tessore⁹⁸, S. Toft^{99,100}, R. Toledo-Moreo¹⁰¹, F. Torradefflot^{40,39}, I. Tutusaus^{3,??,90}, J. Valiviita^{69,70}, T. Vassallo^{5,59}, Y. Wang¹⁰², J. Weller^{30,29}, G. Zamorani²¹, F. M. Zerbi⁹, E. Zucca²¹, V. Allevato³², M. Ballardini^{103,104,21}, A. Boucaud¹⁰⁵, E. Bozzo⁵², C. Burigana^{106,57}, R. Cabanac⁹⁰, M. Calabrese^{107,36}, A. Cappi^{108,21}, T. Castro^{5,11,1,24}, J. A. Escartin Vigo²⁹, L. Gabarra¹³, J. Macias-Perez¹⁰⁹, R. Maoli^{110,37}, J. Martín-Fleitas¹¹¹, N. Mauri^{45,28}, R. B. Metcalf^{75,21}, P. Monaco^{23,5,11,1}, A. A. Nucita^{112,113,114}, M. Pöntinen⁶⁹, I. Risso^{9,25}, V. Scottez^{115,116}, M. Sereno^{21,28}, M. Tenti²⁸, M. Tucci⁵², M. Viel^{1,5,2,11,24}, M. Wiesmann⁶², Y. Akrami^{89,117}, I. T. Andika⁵⁹, G. Angora^{32,103}, M. Archidiacono^{22,61}, F. Atrio-Barandela¹¹⁸, L. Bazzanini^{103,21}, J. Bel¹¹⁹, D. Bertacca^{94,60,54}, M. Bethermin¹²⁰, A. Blanchard⁹⁰, L. Blot^{121,71}, H. Böhringer^{29,59,122}, S. Borgani^{23,1,5,11,24}, M. L. Brown¹²³, S. Bruton¹²⁴, A. Calabro³⁷, F. Caro³⁷, C. S. Carvalho⁹⁷, F. Cogato^{75,21}, A. R. Cooray¹²⁵, S. Davini²⁵, F. De Paolis^{112,113,114}, G. Desprez¹²⁶, A. Díaz-Sánchez¹²⁷, S. Di Domizio^{26,25}, J. M. Diego¹²⁸, V. Durret⁵⁵, M. Y. Elkhashab^{5,11,23,1}, A. Enia²¹, Y. Fang³⁰, A. G. Ferrari²⁸, A. Finoguenov⁶⁹, A. Fontana³⁷, F. Fontanot^{5,1}, A. Franco^{113,112,114}, K. Ganga¹⁰⁵, T. Gasparotto³⁷, E. Gaztanaga^{3,??,129}, F. Giacomini²⁸, F. Gianotti²¹, G. Gozaliasl^{130,69}, A. Gruppuso^{21,28}, C. M. Gutierrez^{46,131}, A. Hall⁶, C. Hernández-Monteagudo^{131,46}, H. Hildebrandt¹³², J. Hjorth⁸², J. J. E. Kajava^{133,134}, Y. Kang⁵², V. Kansal^{135,136}, D. Karagiannis^{103,137}, K. Kiiveri⁹³, J. Kim¹³, C. C. Kirkpatrick⁹³, S. Kruk²⁷, L. Legrand^{138,139}, M. Lembo¹⁴⁰, F. Lepori¹⁴¹, G. Leroy^{142,76}, G. F. Lesci^{75,21}, J. Lesgourgues⁴¹, T. I. Liaudat¹⁴³, M. Magliocchetti⁵⁶, F. Mannucci¹⁴⁴, C. J. A. P. Martins^{145,146}, L. Maurin⁵³, M. Miluzio^{27,147}, A. Montoro^{3,??}, G. Morgante²¹, S. Nadathur¹²⁹, K. Naidoo^{129,67}, A. Navarro-Alsina¹⁰, S. Nesseris⁸⁹, L. Pagano^{103,104}, D. Paoletti^{21,57}, F. Passalacqua^{94,54}, K. Paterson⁶⁷, L. Patrizii²⁸, A. Pisani⁵⁵, D. Potter¹⁴⁸, G. W. Pratt¹⁴, S. Quai^{75,21}, M. Radovich⁶⁰, K. Rojas⁷⁴, W. Roster²⁹, S. Sacquegna¹⁴⁹, M. Sahlén¹⁵⁰, D. B. Sanders⁴⁴, A. Schneider¹⁴⁸, D. Sciotti^{37,38}, E. Sellentin^{151,152}, L. C. Smith¹⁵³, K. Tanidis¹⁵⁴, C. Tao⁵⁵, F. Tarsitano^{155,52}, G. Testera²⁵, R. Teyssier¹⁵⁶, S. Tosi^{26,9,25}, A. Troja^{94,54}, D. Vergani²¹, F. Vernizzi¹⁵⁷, G. Verza^{158,159}, P. Vielzeuf⁵⁵, S. Vinciguerra¹⁹, N. A. Walton¹⁵³, and A. H. Wright¹³²

(Affiliations can be found after the references)

January 29, 2026

Article number, page 1 of 25

ABSTRACT

Accurate modelling of redshift-space distortions (RSD) is essential for maximizing the cosmological information extracted from large galaxy redshift surveys. In preparation for the forthcoming analysis of the *Euclid* spectroscopic data, we investigate three approaches to modelling RSD effects on the power spectrum multipoles of mock H α emission line galaxies. We focus on two one-loop perturbation theory models – the effective field theory (EFT) and velocity difference generator (VDG $_{\infty}$) – which differ in their treatment of the real-to-redshift space mapping on small scales, and a third approach, the BACCO emulator, which adopts a hybrid strategy combining perturbation theory with high-resolution N -body simulations. We assess the ability of these models to recover key cosmological parameters, including the expansion rate h , the cold dark matter density parameter ω_c , and the scalar amplitude A_s , across four redshift bins spanning $0.9 \leq z \leq 1.8$. In each bin, we find that VDG $_{\infty}$ and BACCO outperform the EFT model across all scales up to $k_{\max} \lesssim 0.35 h \text{ Mpc}^{-1}$. While BACCO saturates in constraining power at intermediate scales and higher redshift, the VDG $_{\infty}$ model continues to improve parameter constraints beyond $k_{\max} \gtrsim 0.30 h \text{ Mpc}^{-1}$. The EFT model, although robust on large scales, exhibits significant parameter biases for $k_{\max} \gtrsim 0.25 h \text{ Mpc}^{-1}$, limiting its applicability to *Euclid*-like H α samples. Among the full perturbation theory-based models, the enhanced treatment of small-scale RSD effects in VDG $_{\infty}$ improves cosmological parameter constraints by up to a factor of two.

Key words. Cosmology:large-scale structure of the Universe, cosmological parameters, galaxy bias, redshift space distortions, growth of structure

1. Introduction

The study of the large-scale structure (LSS) through galaxy clustering is one of the primary sources of cosmological information at late times (Colless et al. 2001; Beutler et al. 2012; Le Fèvre et al. 2013; York et al. 2000; Blake et al. 2011; Guzzo et al. 2014; Driver et al. 2011; Dawson et al. 2012; Dawson et al. 2016; DESI Collaboration: Abdul Karim et al. 2025; DESI Collaboration: Adame et al. 2025a,b). Together with weak gravitational lensing (Abbott et al. 2022; DES Collaboration: Abbott et al. 2025; Li et al. 2023; Dark Energy Survey and Kilo-Degree Survey Collaboration et al. 2023), supernovae (Brout et al. 2022), and complementary early-time observations via cosmic microwave background (CMB) experiments (Hinshaw et al. 2013; Planck Collaboration et al. 2020; Louis et al. 2025), galaxy clustering provides invaluable insights into both the geometry and the growth of structures of the Universe, with the potential to disentangle the effects of different dark energy models from potential deviations from general relativity (Alam et al. 2021; DESI Collaboration: Adame et al. 2025a,c; Semenaitė et al. 2022; Carrilho et al. 2023).

Ongoing Stage-IV spectroscopic surveys, such as the Dark Energy Spectroscopic Instrument (DESI; DESI Collaboration: Aghamousa et al. 2016) and *Euclid* (Laureijs et al. 2011; Euclid Collaboration: Mellier et al. 2025), will significantly enhance the information content that can be extracted from the LSS. These experiments reach a relatively uncharted epoch at $1 \leq z \leq 2$, when the Universe was only about half of its current age. Traditionally, information from spectroscopic galaxy surveys is extracted by modelling the 2-point correlation function (2PCF) or its Fourier counterpart, the galaxy power spectrum (Eisenstein et al. 2005; Eisenstein et al. 2007; Beutler et al. 2016; Ivanov & Sibiryakov 2018; Sánchez et al. 2014). The information encapsulated within these statistics is mostly carried by the baryon acoustic oscillation (BAO) peak, determined by the sound horizon at the matter-radiation decoupling era (Peacock et al. 2001; Eisenstein et al. 2005), and redshift-space distortions (RSD), determined by the apparent anisotropic clustering induced by the peculiar velocities of galaxies (Kaiser 1987). Modelling each of these features presents its own unique challenges. For example, BAO analyses rely on reconstruction algorithms to sharpen the acoustic peak by predicting the galaxy velocity field (Zel'dovich 1970; Eisenstein et al. 2007). In turn, RSD are particularly sensitive to nonlinear physics, requiring a complex modelling of the mildly nonlinear regime to accurately describe the observed clustering signal.

* e-mail: bcamacho@sissa.it

Spectroscopic galaxy surveys do not provide direct access to the real-space position of galaxies, but rather to their angular position and redshift. The latter is sensitive not only to the recession velocity, due to the expansion of the Universe, but also to the galaxy peculiar velocity, which is sourced by its gravitational interaction with its surrounding. As a consequence, the observed redshift-space galaxy distribution corresponds to a distorted version of the underlying real-space distribution (Kaiser 1987; Hamilton 1992; Fisher 1995; Scoccimarro et al. 1999; Scoccimarro 2004; Taruya et al. 2010; Senatore & Zaldarriaga 2014; Perko et al. 2016), leading to a complex mapping involving both the density and velocity fields. Hence, accurately describing the real- to redshift-space mapping is critical to capture the effect of RSD and reliably estimate the growth rate of cosmic structures.

In the context of galaxy clustering, models based on perturbation theory (hereafter PT, Bernardeau et al. 2002) are powerful tools for extracting cosmological information from full-shape measurements of the anisotropic galaxy power spectrum. Perturbative methods can be employed to model different, yet intertwined, effects that contribute to the shaping of the observed galaxy density field. First, it can be used to describe the nonlinear evolution of the dark matter density field over mildly nonlinear scales. Second, it can model the relationship between the galaxy and matter density fields (usually refereed as galaxy bias expansion, Szalay 1988; Coles 1993; Fry & Gaztanaga 1993; Scoccimarro et al. 2001; Smith et al. 2007; Manera et al. 2010; Desjacques et al. 2010; Frusciante & Sheth 2012; Schmidt et al. 2013), which is essential as we can only observe biased tracers of the underlying dark matter field. Finally, RSD and ultraviolet (UV) limit effects become more important when approaching the strong nonlinear regime (around $k \sim 0.20 h \text{ Mpc}^{-1}$), where PT begins to break down. These effects introduce significant distortions in the shape and amplitude of the power spectrum and their impact is modulated by a set of extra parameters, usually denoted as counterterms (Senatore & Zaldarriaga 2014; Desjacques et al. 2018b; Ivanov et al. 2020; Pueblas & Scoccimarro 2009). Lastly, contributions from small scales (beyond $k = 0.20 h \text{ Mpc}^{-1}$), coupled with larger scales and acting as a stochastic field, must be modelled as noise parameters (Dekel & Lahav 1999; Taruya & Soda 1999; Matsubara 1999). Traditionally, this picture is complemented with a technique called infrared (IR) resummation, which serves as a way to model large-scale bulk flows smearing the BAO peak (Eisenstein et al. 2007; Baldauf et al. 2015; Blas et al. 2016).

In recent years, different approaches to model the real- to redshift-space mapping have emerged. Among them, one of the

most successful frameworks is the effective field theory of large-scale structure (EFT), which treats both density and velocity fields in a fully perturbative way (Carrasco et al. 2012; Senatore & Zaldarriaga 2015; Perko et al. 2016; Ivanov et al. 2020; d’Amico et al. 2020). This framework accounts for the small-scale RSD signal by expanding the velocity difference moment generating function and introducing a set of counterterms to reproduce its effect at leading- and next-to-leading order in the power spectrum (Pueblas & Scoccimarro 2009; Senatore & Zaldarriaga 2014; Desjacques et al. 2018b; Ivanov et al. 2020). Alternatively, in an equally successful class of models, the moment generating function can be described analytically using a physically-motivated functional form, which tries to reproduce the pairwise velocity distribution at some fixed physical separation (Taruya et al. 2010; Sánchez et al. 2016). Finally, beyond these purely analytical approaches, hybrid models have shown considerable success recently (Zennaro et al. 2023; Aricò et al. 2022; Kokron et al. 2021; Pellejero Ibañez et al. 2022). These types of models keep the traditional expansion of the redshift-space galaxy density field, but emulate each of the individual components of the expansion from high-resolution N -body simulations.

In this work, we aim at comparing three different modelling approaches for the anisotropic galaxy power spectrum, all of them based on the one-loop galaxy bias expansion, but differing mainly in how they perform the real- to redshift-space mapping. Two of these models are fully analytical, falling in one of the two categories described above, while the third one is based on a hybrid perturbative framework. As a testing ground for the different models, we use a set of data vectors derived from mock galaxy catalogues designed to reproduce the clustering properties of the $\text{H}\alpha$ sample targeted by *Euclid* (Pozzetti et al. 2016).

The range of validity of each model is quantified through three complementary performance metrics. First, we calculate the figure of bias (FoB) to quantify the accuracy of the model in recovering the input parameters. Second, we compute the figure of merit (FoM) to measure the statistical power of the model in constraining cosmological parameters. Third, we evaluate the goodness of fit (p -value) to assess how well the best-fit model matches the input data vectors. These metrics are computed for each model as a function of the maximum wave mode, k_{\max} , included in the fit. Our analysis focuses on the recovery of the dimensionless Hubble parameter h , defined in terms of the Hubble constant H_0 as $H_0 = 100 h \text{ km s}^{-1} \text{ Mpc}^{-1}$, the cold dark matter density parameter $\omega_c \equiv \Omega_c h^2$, and the scalar amplitude A_s .

This work is part of a series of validation tests to identify the optimal modelling framework for galaxy clustering measurements within the Euclid Consortium. In Euclid Collaboration: Pezzotta et al. (2024) we perform an equivalent comparison for modelling the galaxy power spectrum in real space, while in Euclid Collaboration: Pardede et al. (in prep.) we extend it to the galaxy bispectrum analysis (both in real and redshift space). Likewise, equivalent comparisons in configuration space are presented in Euclid Collaboration: Kärcher et al. (2026) in terms of the 2PCF, with the extension to higher-order statistics presented in Euclid Collaboration: Guidi et al. (2025) and Euclid Collaboration: Pugno et al. (in prep.), for the real- and redshift-space case, respectively.

This paper is structured as follows. We begin by describing the data vectors and covariance matrices of data noise used for testing the models in Sect. 2. In Sect. 3 we describe the three modelling frameworks tested in this work. In Sect. 4 we describe the performance metrics and fitting strategies employed in the analysis. In Sect. 5 we validate the two fully perturbative models

Table 1. Cosmological parameters of the Flagship I simulations. The table shows the values of the Hubble parameter h , the physical densities of cold dark matter and baryons (ω_c and ω_b), the total neutrino mass M_ν , the scalar amplitude A_s , and the index n_s of the primordial power spectrum.

h	ω_c	ω_b	M_ν [eV]	$10^9 A_s$	n_s
0.67	0.121203	0.0219961	0	2.09	0.97

to ensure a fair comparisons with the hybrid model. The complete comparison between the performance of the three models, focusing on their range of validity and constraining power, is presented in Sect. 6. Finally we conclude by highlighting the key findings of this work in Sect. 7.

2. Data

2.1. Euclid simulations

To study the performance of the different models, we use dedicated mock catalogues of $\text{H}\alpha$ galaxies with a flux limit $f_{\text{H}\alpha} = 2 \times 10^{-16} \text{ erg cm}^{-2} \text{ s}^{-1}$, to match the primary spectroscopic sample of the *Euclid* mission. These catalogues are based on the Flagship I N -body simulation (Potter et al. 2017),¹ which used the PKDGRAV3 algorithm to evolve two trillion dark matter particles within a comoving box of size $L_{\text{box}} = 3780 h^{-1} \text{ Mpc}$ and with a particle mass resolution of $m_p \sim 2.398 \times 10^9 h^{-1} M_\odot$. Such combination of large volume and high mass resolution is unique, and it enables to accurately resolve haloes hosting the majority of the expected *Euclid* $\text{H}\alpha$ sample, whose typical mass is of the order of few $10^{10} h^{-1} M_\odot$, within a volume exceeding the nominal final-mission volume of *Euclid* by several times. The fiducial cosmology of the simulation is presented in Table 1 (see discussion in Appendix A of Euclid Collaboration: Pezzotta et al. 2024). In agreement with the real-space analysis in Euclid Collaboration: Pezzotta et al. (2024), we used the same four snapshots of $\text{H}\alpha$ galaxies in the redshift range $0.9 < z < 1.8$.

In this paper, we neglect the impact of different contaminants and systematic errors that may affect *Euclid* observations, such as target incompleteness, purity of the sample, and the impact of the angular footprint and radial selection function.² In addition, we focus our analysis only on the Model 3 halo occupation distribution (HOD) sample described in Pozzetti et al. (2016),³ since it displays a lower number density that more closely matches the one expected systematic-free sample of $\text{H}\alpha$ galaxies.

The total number of galaxies in each comoving snapshot, their number density, and the scale k_{sn} at which the Poissonian shot-noise contribution reaches the same amplitude of the power spectrum monopole ($\ell = 0$), that is, $\bar{n} P_0 \sim 1$, are listed in Table 2.

2.2. Power spectrum multipole measurements

From the $\text{H}\alpha$ mocks, we compute the Legendre multipoles of the galaxy power spectrum using the publicly available Power14

¹ Similarly to Euclid Collaboration: Pezzotta et al. (2024), we use the Roman numeral ‘I’ to differentiate it from its more recent version, that is, Flagship II (Euclid Collaboration: Castander et al. 2025).

² For a description of the *Euclid* visibility mask and observational systematic effects in *Euclid*, see Euclid Collaboration: Granett et al. (in prep.) and Euclid Collaboration: Monaco et al. (2025).

³ For the specific shape of the implemented HOD see Sect. 2.1 in Euclid Collaboration: Pezzotta et al. (2024).

Table 2. Specifications of the Model 3 H α mock galaxy samples used throughout this paper. The columns indicate the redshift of the sample z , the total number of galaxies N_g , the mean number density \bar{n} , and the scale k_{sn} at which the Poissonian shot-noise contribution equals the signal of the $\ell = 0$ galaxy power spectrum multipole. Lastly, η indicates the normalization factor to scale the Flagship covariance to *Euclid*-like errors, as explained in Sect. 2.3.

z	N_g	$\bar{n} [h^3 \text{Mpc}^{-3}]$	$k_{\text{sn}} [h \text{Mpc}^{-1}]$	η
0.9	110 321 755	0.0020	0.50	6.6
1.2	55 563 490	0.0010	0.42	5.9
1.5	31 613 213	0.0006	0.30	5.3
1.8	16 926 864	0.0003	0.26	3.3

code,⁴ which calculates power spectra in periodic cubic boxes employing the flat-sky approximation. This allows us to measure the RSD signal along each of the three coordinate axes (x, y, z).

The fundamental frequency of the power spectrum measurements is determined from the simulation box size as $k_F \equiv 2\pi/L_{\text{box}} \sim 0.0016 h \text{Mpc}^{-1}$. In contrast, the maximum wave mode is defined by the Nyquist frequency, which for a density grid with N_{grid} linear bins is given by $k_{\text{Nyq}} \equiv \pi N_{\text{grid}}/L_{\text{box}}$. For the three different directions, we adopt the same grid resolution $N_{\text{grid}} = 1024$, which leads to $k_{\text{Nyq}} \sim 0.85 h \text{Mpc}^{-1}$. These quantities define the wave mode range of our measurements, $k \in [k_F, k_{\text{Nyq}}]$, which we sample using a linear binning of width $\Delta k = k_F$.

We obtain measurements of the power spectrum multipoles using each of the three directions of the cubic box as line of sight. In redshift space, these three measurements are highly correlated; albeit they have different line-of-sight velocity contributions, they share the same density field (for a comprehensive discussion on how these effects are coupled together, see Smith et al. 2021). Instead of averaging the power spectra over the three axes – this would unevenly weight the density field (common to all directions) and the velocity field – we use only the measurement along the axis that shows the best goodness of fit when compared to the average over the three axes. Precisely, for a given snapshot at redshift z , we define $\chi^2 \equiv (\chi_x^2, \chi_y^2, \chi_z^2)$, where each element χ_i^2 corresponds to the error-weighted mean square difference between the averaged multipoles and the ones with line of sight parallel to the i -th axis. We find that $\chi^2(0.9) = (0.59, 0.55, 0.50)$, $\chi^2(1.2) = (0.58, 0.57, 0.50)$, $\chi^2(1.5) = (0.60, 0.53, 0.48)$, and $\chi^2(1.8) = (0.50, 0.51, 0.51)$. We therefore adopt the z axis as our baseline data vector, since it provides the lowest χ^2 across most of our samples.

In Fig. 1 we show the first three even Legendre multipoles along the z axis for each of the considered redshifts. Additionally, we show the Poissonian shot-noise contribution P_{sn} to highlight the transition to the shot-noise dominated scales. At low redshift, shot-noise remains negligible up to $k = 0.5 h \text{Mpc}^{-1}$, while at high redshift it matches the monopole amplitude already at $k = 0.26 h \text{Mpc}^{-1}$, as indicated in Table 2.

2.3. Power spectrum covariance

The covariance matrices of the power spectrum multipoles are generated using a theoretical model based on the Gaussian predictions, as described in Grieb et al. (2016). In practice, we

compute the diagonal and cross-diagonal covariance terms composed of all the possible combinations among the multipole orders $\ell = (0, 2, 4)$. For computing the theoretical covariance we use the nonlinear power spectra obtained from iteratively fitting the multipole measurements at fixed cosmology and high k_{max} . The fit is repeated until converging to a stable set of values for the model parameters. This partially accounts for non-Gaussian contributions to the covariance. Other non-Gaussian terms are neglected for simplicity, since we are using a box geometry, and window effects are expected to be negligible (Blot et al. 2019; Wadekar et al. 2020).

Unless otherwise stated, the covariance matrix is computed assuming the full volume of the Flagship I simulation, $V_{\text{box}} = (3.78 h^{-1} \text{Gpc})^3$. The error bars displayed in Fig. 1 correspond to the Flagship simulation volume and illustrate the extreme precision of the measurements implemented in this work. Notice that for scales $k > 0.1 h \text{Mpc}^{-1}$ the error over the signal is smaller than 10^{-2} for all redshift bins. Additionally, to assess the expected constraining power and model performance with more realistic errors, tiled to the one expected from the full *Euclid* mission, we rescale the Flagship covariance matrices C , by the ratio between the volume of the Flagship I comoving outputs, V_{box} , and the volume of the corresponding *Euclid* redshift bin, V_{shell} . This approach allows us to define a scaling factor

$$\eta = \frac{V_{\text{box}}}{V_{\text{shell}}}, \quad (1)$$

which is latter employed to compute a covariance C_{shell} for a given shell as

$$C_{\text{shell}} = \eta C. \quad (2)$$

In order to derive volume factors η we follow the specifications defined in Euclid Collaboration: Blanchard et al. (2020, see also Euclid Collaboration: Pezzotta et al. 2024). We assume four non-overlapping redshift bins, centred at the snapshot redshift, with a width $\Delta z = (0.2, 0.2, 0.2, 0.3)$ and a total survey area of $15\,000 \text{ deg}^2$. The η values are shown in the last column of Table 2.

3. Theoretical models

In this study, we consider three different modelling frameworks for the redshift-space galaxy power spectrum multipoles. Two of these are based on Eulerian perturbation theory (EPT) and differ in their treatment of small-scale RSD. The first model uses a fully perturbative expansion of the real- to redshift-space mapping, whereas the second replaces this expansion with an analytic function derived from the resummation of various nonlinear terms. The third model is hybrid, uses a Lagrangian expansion of the redshift-space galaxy density field, but each term is measured and emulated using high-resolution N -body simulations (see Sec. 3.2).

3.1. Perturbation theory models

3.1.1. Redshift-space mapping

The mapping from the real-space position \mathbf{x} of a given object to its observed redshift-space position \mathbf{s} is sourced by the peculiar velocity of the object. In the plane-parallel approximation this mapping is given as

$$\mathbf{s} = \mathbf{x} - f u_z(\mathbf{x}) \hat{z}, \quad (3)$$

⁴ <https://github.com/sefusatti/PowerI4>.

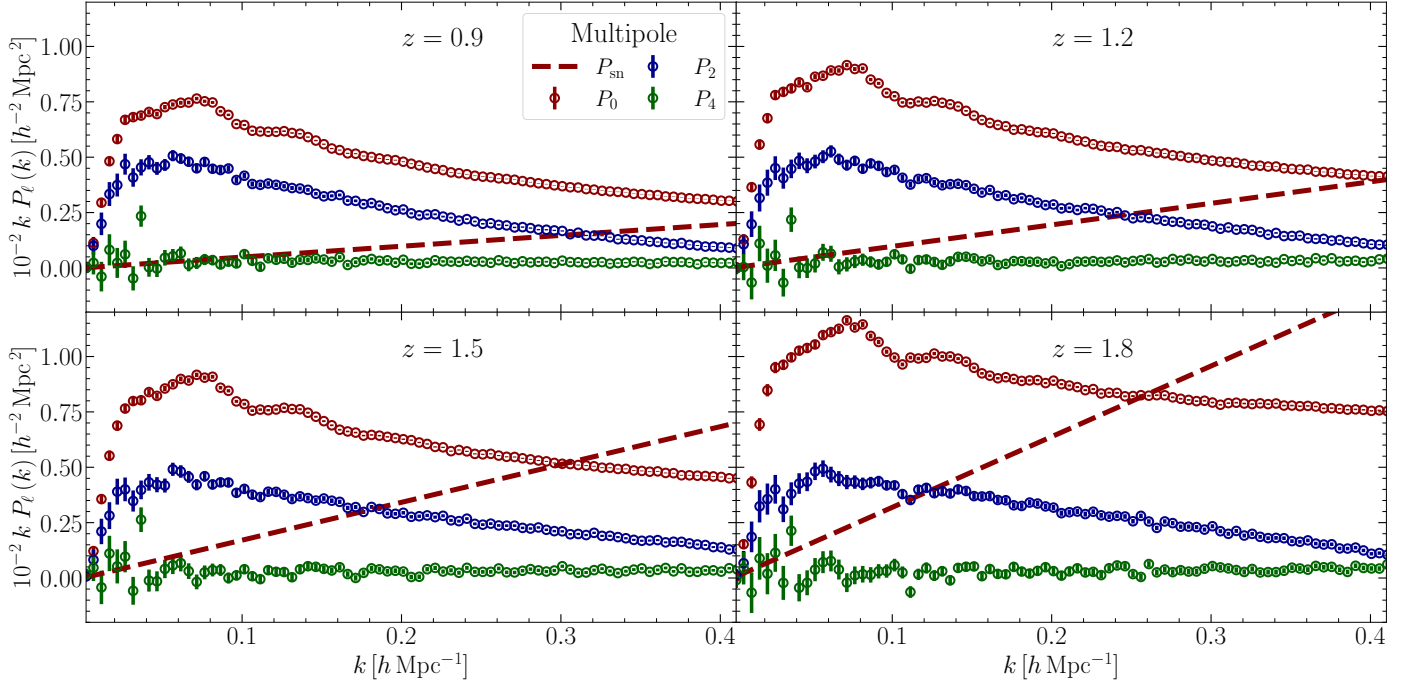


Fig. 1. Power spectrum Legendre multipoles as measured from the Model 3 HOD samples built on the Flagship I comoving snapshots. Markers show each multipole along the z axis, with different colours marking different multipoles as indicated in the legend. The error bars correspond to the Gaussian covariance for a comoving volume corresponding to the full box of the Flagship I simulation, as described in Sect. 2. Dashed red line refers to the Poissonian shot-noise contribution P_{sn} . For visualization purposes, we show only one out of three data points.

where $u_z(\mathbf{x})$ is the component of the normalised velocity field along the line of sight, defined through $u_z(\mathbf{x}) \equiv v_z(\mathbf{x})/(-f \mathcal{H})$, where f refers to the linear growth rate and \mathcal{H} is the comoving Hubble parameter.

The redshift-space density field δ^s in Fourier space is then (Scoccimarro et al. 1999)

$$\delta^s(\mathbf{k}) = \int d^3x e^{-ik \cdot x} e^{ifk_z u_z(x)} [\delta(\mathbf{x}) + f \nabla_z u_z(\mathbf{x})], \quad (4)$$

where the term in squared brackets captures the large-scale Kaiser effect (Kaiser 1987), while the exponential prefactor generates the small-scale Finger-of-God (FoG) suppression.

The corresponding redshift-space power spectrum is (Scoccimarro et al. 2004)

$$P^s(k, \mu) = \int d^3r e^{-ik \cdot r} \left\langle e^{ifk\mu \Delta u_z} \times [\delta(\mathbf{x}) + f \nabla_z u_z(\mathbf{x})] [\delta(\mathbf{x}') + f \nabla_z u_z(\mathbf{x}')] \right\rangle, \quad (5)$$

where $\Delta u_z \equiv u_z(\mathbf{x}) - u_z(\mathbf{x}')$, $\mathbf{r} \equiv \mathbf{x} - \mathbf{x}'$ and μ is the cosine of the angle between the pair separation vector and the line of sight.

3.1.2. EFT and VDG_∞

From Eq. (5), we distinguish two approaches. The EFT model (Senatore & Zaldarriaga 2014; Perko et al. 2016), that expands the exponential prefactor $e^{ifk\mu \Delta u_z}$ and describes the nonlinear density and velocity fields perturbatively, with counterterms absorbing small-scale FoG damping and residual UV deficiencies. The EFT anisotropic galaxy power spectrum is written as

$$P_{\text{gg, EFT}}(\mathbf{k}) = P_{\text{gg, SPT}}^{\text{tree}}(\mathbf{k}) + P_{\text{gg, SPT}}^{\text{1-loop}}(\mathbf{k}) + P_{\text{gg}}^{\text{stoch}}(\mathbf{k}) + P_{\text{gg}}^{\text{ctr}}(\mathbf{k}), \quad (6)$$

where the terms represent the tree-level and one-loop standard perturbation theory (SPT) contributions, stochastic noise, and counterterms, respectively.

And the velocity difference-generating function at infinity (VDG_∞) model, that describes the contribution from virialised velocities through an effective damping function, with the power spectrum given by

$$P_{\text{gg, VDG}_\infty}(\mathbf{k}) = W_\infty(\mathbf{k}) \left[P_{\text{gg, SPT}}^{\text{tree}}(\mathbf{k}) + P_{\text{gg, SPT}}^{\text{1-loop}}(\mathbf{k}) - \Delta P(\mathbf{k}) + P_{\text{gg}}^{\text{ctr, LO}}(\mathbf{k}) \right] + P_{\text{gg}}^{\text{stoch}}(\mathbf{k}), \quad (7)$$

where W_∞ denotes the effective damping function for modelling RSD, and is derived by taking the VDG_∞ , leading to

$$W_\infty(\lambda) = \frac{1}{\sqrt{1 - \lambda^2 a_{\text{vir}}^2}} \exp \left(\frac{\lambda^2 \sigma_v^2}{1 - \lambda^2 a_{\text{vir}}^2} \right), \quad (8)$$

with $\lambda = -i f k \mu$, and a_{vir} being a free parameter to modulate the kurtosis of the velocity difference distribution (Scoccimarro et al. 2004; Eggemeier et al. 2025). The term $\Delta P(\mathbf{k})$ corrects for extra contributions generated by the perturbative expansion of the velocity difference-generating function (VDG) in the EFT approach (Eggemeier et al. 2023, 2025).

3.1.3. Galaxy bias expansion and stochasticity

The galaxy overdensity δ_g is related to the dark matter density field δ through a bias expansion. Up to cubic order in δ , and adopting the parametrisation from Eggemeier et al. (2019), we have (keeping only terms relevant to the power spectrum):

$$\delta_g(\mathbf{x}) = b_1 \delta(\mathbf{x}) + \frac{b_2}{2} \delta^2(\mathbf{x}) + \gamma_2 \mathcal{G}_2(\mathbf{x}) + \gamma_{21} \mathcal{G}_{21}(\mathbf{x}) + b_{\nabla^2 \delta} \nabla^2 \delta(\mathbf{x}) + \varepsilon_g(\mathbf{x}), \quad (9)$$

where b_1 and b_2 are the linear and quadratic biases, γ_2 and γ_{21} modulate the impact of the non-local-in-matter-density operators \mathcal{G}_2 and \mathcal{G}_{21} , and $b_{\nabla^2\delta}$ is the higher-derivative bias. Explicit expressions for the P_{gg} spectra in Eqs. (6,7) obtained from the expansion in Eq. (9) are given in Eggemeier et al. (2019).

The stochastic field ε_g is uncorrelated with the large-scale density field, $\langle \varepsilon_g \delta \rangle = 0$, and its power spectrum at large scales is expanded as (Desjacques et al. 2018a; Eggemeier et al. 2021)

$$P_{\varepsilon_g \varepsilon_g}(k) = \frac{1}{\bar{n}} \left(N_0^P + N_{20}^P k^2 + \dots \right), \quad (10)$$

where \bar{n} represents the mean number density of the tracer population, whereas N_0^P and N_{20}^P are two free parameters modulating the constant and leading-order scale-dependent stochastic correction to take into account deviations from purely Poisson shot noise and exclusion effects. An additional stochastic component from the redshift-space mapping, $\varepsilon_{\nabla_z u_z}$, contributes a term (Eggemeier et al. 2025)

$$P_{\varepsilon_g \varepsilon_{\nabla_z u_z}}(k, \mu) = \frac{N_{22}^P}{\bar{n}} \mathcal{L}_2(\mu) k^2 + \dots, \quad (11)$$

where $\mathcal{L}_2(\mu)$ denotes the second-order Legendre polynomial. The total stochastic power spectrum is then

$$P_{gg}^{\text{stoch}}(k, \mu) = P_{\varepsilon_g \varepsilon_g}(k) + P_{\varepsilon_g \varepsilon_{\nabla_z u_z}}(k, \mu). \quad (12)$$

3.1.4. Counterterms

To mitigate the breakdown of PT on small scales, both the EFT and VDG_∞ models introduce a set of counterterms. At leading order we parametrise them as

$$P_{gg}^{\text{ctr,LO}}(k, \mu) = -2 \sum_{n=0}^2 c_{2n} \mathcal{L}_{2n}(\mu) k^2 P_L(k), \quad (13)$$

where P_L corresponds to the linear matter power spectrum. The angular dependence of the counterterms is parametrised in terms of the Legendre polynomials of order $2n$ – in practice it introduces the parameters c_0 , c_2 , and c_4 , with adjustable amplitude. Since the contribution from higher-derivative bias scales identically to the c_0 counterterm, we let c_0 absorb the dependence on $b_{\nabla^2\delta}$.

The VDG_∞ models has hence 3 counter-terms. For the EFT model, we include an extra next-to-leading order term with free amplitude c_{nlo}

$$P_{gg}^{\text{ctr,NLO}}(k, \mu) = c_{\text{nlo}} (\mu k f)^4 P_{gg, \text{SPT}}^{\text{tree}}(k). \quad (14)$$

The total counterterm correction for the EFT model is therefore

$$P_{gg}^{\text{ctr}}(k, \mu) = P_{gg}^{\text{ctr,LO}}(k, \mu) + P_{gg}^{\text{ctr,NLO}}(k, \mu). \quad (15)$$

3.1.5. Infrared resummation and bias relations

To account for the smearing of BAO features by large-scale bulk flows (Crocce & Scoccimarro 2006; Crocce & Scoccimarro 2008), we adopt an IR resummation formalism, where the linear power spectrum is decomposed into a smooth component P_{nw} and a wiggly component P_w : $P_L(k) = P_{\text{nw}}(k) + P_w(k)$. Then the IR-resummed power spectrum is computed as the sum of the smooth and the anisotropically damped wiggly component, following the treatment in Ivanov & Sibiryakov (2018).

Finally, for the EPT models, we assess the validity of physically-motivated relations to reduce the number of free parameters. We use the co-evolution relations for the non-local biases (Fry 1996; Chan et al. 2012)

$$\gamma_{21}^{\text{coev}} = \frac{2}{21} (b_1 - 1) + \frac{6}{7} \gamma_2, \quad (16)$$

and for γ_2 we employ the excursion set relation (Eggemeier et al. 2020):

$$\gamma_2^{\text{ex-set}} = 0.524 - 0.547 b_1 + 0.046 b_1^2. \quad (17)$$

3.2. Hybrid model: the BACCO emulator

The hybrid approach (Modi et al. 2020; Pellejero Ibañez et al. 2022) comprises two components: a transformation from Lagrangian to Eulerian coordinates using the displacement field $\psi(\mathbf{q})$ from N -body simulations, and a Lagrangian bias model $F[\delta_L(\mathbf{q})]$. We adopt a second-order perturbative expansion for the bias model as (Matsubara 2008; Desjacques et al. 2018a)

$$F[\delta_L(\mathbf{q})] = 1 + b_1^L \delta_L(\mathbf{q}) + b_2^L [\delta_L^2(\mathbf{q}) - \langle \delta_L^2(\mathbf{q}) \rangle] + b_s^L [s^2(\mathbf{q}) - \langle s^2(\mathbf{q}) \rangle] + b_\nabla^L \nabla^2 \delta_L(\mathbf{q}), \quad (18)$$

where $s^2 \equiv s_{ij} s^{ij}$ is the scalar traceless tidal tensor. The Eulerian galaxy density field is then

$$1 + \delta_g(\mathbf{x}) = \int d^3 q F[\delta_L(\mathbf{q})] \delta_D[\mathbf{x} - \mathbf{q} - \psi(\mathbf{q})], \quad (19)$$

where δ_D represents the Dirac delta function.

The real- to redshift-space mapping is implemented by modifying the displacement field (Pellejero Ibañez et al. 2022)

$$\psi(\mathbf{q}) \rightarrow \psi(\mathbf{q}) + \frac{v_z(\mathbf{x})}{\mathcal{H}} \hat{z}, \quad (20)$$

where the velocity field $\mathbf{v}(\mathbf{x})$ is constructed from velocities measured in N -body simulations.

To account for intra-halo satellite velocities, we introduce a damping function (following Orsi & Angulo 2018) – as in Eq. (7), it plays the role of damping the final galaxy power spectrum – with shape

$$W(k, \mu) \equiv \left[(1 - f_{\text{sat}}) + f_{\text{sat}} \frac{\lambda_{\text{sat}}^2}{\lambda_{\text{sat}}^2 + k^2 \mu^2} \right]^2. \quad (21)$$

Here f_{sat} is the satellite fraction and λ_{sat} their velocity dispersion. Lastly, the stochastic component is modelled as $P_{gg}^{\text{stoch}}(k, \mu) = P_{\varepsilon_g \varepsilon_g}(k)$, with the same shape as in Eq. (10).

3.3. Alcock–Paczynski distortions

To account for geometric distortions due to discrepancies between the true and the assumed fiducial cosmology, we apply Alcock–Paczynski (AP) corrections. The line-of-sight and transverse distortion parameters are defined as the ratios of the Hubble parameter (H) and the comoving transverse distance (D_M) in the true and fiducial cosmologies

$$q_{\parallel} \equiv \frac{H'(z)}{H(z)}, \quad q_{\perp} \equiv \frac{D_M(z)}{D_M'(z)}, \quad (22)$$

where fiducial values are indicated by primed quantities.

The power spectrum multipoles in the fiducial cosmology are computed as (Ballinger et al. 1996)

$$P'_\ell(k') = \frac{2\ell+1}{2q_\perp^2 q_\parallel} \int_{-1}^1 d\mu' \mathcal{L}_\ell(\mu') P[k(k', \mu'), \mu(\mu')] , \quad (23)$$

with the wavenumber and angle mapping given by

$$k = \frac{k'}{q_\perp} \left[1 + \mu'^2 (F^{-2} - 1) \right]^{1/2} , \quad (24)$$

$$\mu = \frac{\mu'}{F} \left[1 + \mu'^2 (F^{-2} - 1) \right]^{-1/2} , \quad (25)$$

where $F \equiv q_\parallel / q_\perp$.

4. Analysis procedure

In this section we outline the Bayesian likelihood analysis. We describe the parameter space and priors, and the performance metrics used to evaluate each model's accuracy, precision, and goodness of fit as a function of scale cut.

4.1. Likelihood analysis

We sample the posterior distribution using the nested sampling algorithm `MultiNest` via its Python wrapper `PyMultiNest` (Skilling 2006),⁵ configured with 600 live points, a sampling efficiency of 0.5, and an evidence tolerance of 0.3. Posteriors are analyzed with `getdist` (Lewis 2025).⁶

We assume a Gaussian likelihood, which up to a normalisation constant can be expressed as:

$$-2 \ln \mathcal{L}(\boldsymbol{\theta}) = \sum_{i,j=1}^{N_{\text{bins}}} \left[P_i^{\text{th}}(\boldsymbol{\theta}) - P_i^{\text{data}} \right] C_{ij}^{-1} \left[P_j^{\text{th}}(\boldsymbol{\theta}) - P_j^{\text{data}} \right] , \quad (26)$$

where P^{th} and P^{data} are the theoretical and measured power spectrum multipoles, C_{ij} is the data covariance (Sect. 2.3), and N_{bins} is the total number of k bins. We test each model up to a maximum wave mode k_{max} , applying a scale cut of $(k_{\text{max}}, k_{\text{max}} - \Delta k, k_{\text{max}} - 2\Delta k)$ for the (P_0, P_2, P_4) multipoles, with $\Delta k = 0.05h^{-1}$ Mpc in our baseline analysis.

To achieve the required $O(10^6)$ model evaluations, we use fast emulators: the `COMET` code (Eggemeier et al. 2023; Pezzotta et al. 2025)⁷ for the EPT models and the `BACCO` emulator (Pellejero Ibañez et al. 2023)⁸ for the hybrid approach, both providing evaluations in ~10 ms.

4.2. Parameter priors

We sample the cosmological parameters (h, ω_c, A_s) with broad flat priors (Table 3). The spectral index n_s and baryon density ω_b are fixed to their fiducial values.

The EPT model parameter space includes 11 nuisance parameters: ten shared parameters ($b_1, b_2, \gamma_2, \gamma_{21}, c_0, c_2, c_4, N_0^P, N_{20}^P, N_{22}^P$) and one model-specific parameter (c_{nlo} for EFT; a_{vir} for VDG_∞).

The hybrid `BACCO` bias basis can be related to the EPT basis via the approximate relations (Zennaro et al. 2022):

$$b_1 = b_1^{\mathcal{L}} + 1 , \quad b_2 = 2b_2^{\mathcal{L}} + \frac{8}{21}b_1^{\mathcal{L}} , \quad \gamma_2 = b_{s^2}^{\mathcal{L}} - \frac{2}{7}b_1^{\mathcal{L}} . \quad (27)$$

Table 3. List of parameters varied in our analysis. The first and second columns indicate the parameter type and name, while the third column reports the prior ranges adopted. The symbol \mathcal{U} denotes a uniform distribution, with the minimum and maximum values specified in square brackets. Since the emulation is performed in terms of σ_8 , the `BACCO` prior on A_s is flat (as in the EPT models), but its boundaries are determined by the emulated values σ_8^{min} and σ_8^{max} . In the table, we explicitly display these σ_8 limits in the prior column.

	Parameter	Prior
Eulerian bias expansion		
Cosmology	h	$\mathcal{U}[0.6, 0.8]$
	$10^9 A_s$	$\mathcal{U}[0.85, 2.95]$
	ω_c	$\mathcal{U}[0.085, 0.15]$
Bias	b_1	$\mathcal{U}[0.25, 4]$
	b_2	$\mathcal{U}[-5, 10]$
	γ_2	$\mathcal{U}[-4, 4]$ or fix to Eq. (17)
	γ_{21}	$\mathcal{U}[-8, 8]$ or fix to Eq. (16)
Counterterms	$c_0 [(\text{Mpc}/h)^2]$	$\mathcal{U}[-500, 500]$
	$c_2 [(\text{Mpc}/h)^2]$	$\mathcal{U}[-500, 500]$
	$c_4 [(\text{Mpc}/h)^2]$	$\mathcal{U}[-500, 500]$
EFT only	$c_{\text{nlo}} [(\text{Mpc}/h)^4]$	$\mathcal{U}[-500, 500]$
VDG_∞ only	$a_{\text{vir}} [\text{Mpc}/h]$	$\mathcal{U}[0, 20]$
Shot-noise	N_0^P	$\mathcal{U}[-1, 2]$
	$N_{20}^P [(\text{Mpc}/h)^2]$	$\mathcal{U}[-500, 500]$
	$N_{22}^P [(\text{Mpc}/h)^2]$	$\mathcal{U}[-500, 500]$
Hybrid Lagrangian bias expansion		
Cosmology	h	$\mathcal{U}[0.6, 0.8]$
	A_s	$\mathcal{U}[\sigma_8^{\text{min}} = 0.65, \sigma_8^{\text{max}} = 0.9]$
	Ω_c	$\mathcal{U}[0.23, 0.4]$
Bias	$b_1^{\mathcal{L}}$	$\mathcal{U}[0.2, 2]$
	$b_2^{\mathcal{L}}$	$\mathcal{U}[-2, 2]$
	$b_{s^2}^{\mathcal{L}}$	$\mathcal{U}[-2, 2]$
	$b_{\nabla^2 \delta}^{\mathcal{L}} [(\text{Mpc}/h)^2]$	$\mathcal{U}[-4, 4]$
FoG	f_{sat}	$\mathcal{U}[0, 1]$
	λ_{sat}	$\mathcal{U}[0, 2]$
Shot-noise	N_0^P	$\mathcal{U}[-1, 1]$
	$N_{20}^P [(\text{Mpc}/h)^2]$	$\mathcal{U}[-3, 3]$

While `BACCO` does not explicitly include γ_{21} as a free parameter, this term is generated during the advection to Eulerian space. The hybrid model shares six nuisance parameters with the EPT models (assuming the γ_{21} relation in Eq. 16), plus N_0^P and N_{20}^P . Its higher-derivative term $b_{\nabla^2 \delta}^{\mathcal{L}}$ partially reproduces the c_0 counterterm, while the damping parameters f_{sat} and λ_{sat} are specific to its treatment of FoG effects.

Nuisance parameters are varied under broad flat priors (Table 3), providing a conservative setup to avoid prior-driven biases. The only exceptions are configurations validating bias relations (Sect. 3.1.5), where γ_2 and γ_{21} are fixed to Eqs. (17) and (16), respectively. Prior ranges differ between the EPT models

⁵ <http://johannesbuchner.github.io/PyMultiNest>

⁶ <https://getdist.readthedocs.io>

⁷ <https://comet-emu.readthedocs.io>

⁸ <https://bacco.dipc.org/emulator.html>

and BACCO, but are sufficiently wide that posteriors do not hit boundaries at intermediate scales. We explore potential boundary effects at large scales in Sect. 6.1.

4.3. Performance metrics

We assess model performance using three metrics.

4.3.1. Figure of bias

We quantify parameter recovery bias using the figure of bias (FoB)

$$\text{FoB}(\theta) \equiv \left[(\langle \theta \rangle - \theta_{\text{fid}})^T S^{-1}(\theta) (\langle \theta \rangle - \theta_{\text{fid}}) \right]^{\frac{1}{2}}, \quad (28)$$

where $\langle \theta \rangle$ is the posterior mean, θ_{fid} are the fiducial values, and $S(\theta)$ is the parameter covariance. We compute the FoB for $\theta = (h, A_s, \omega_c)$, marginalizing over nuisance parameters.

For a 3-parameter FoB, the 68% and 95% confidence limits correspond to values of 1.88 and 2.83, respectively. For analyses with *Euclid*-like covariances, we rescale the 68% and 95% thresholds by $1/\sqrt{\eta}$, where η is the volume ratio between the Flagship box and the *Euclid*-like shell (Table 2).

4.3.2. Figure of merit

We evaluate constraining power using the figure of merit (FoM) (Wang 2008)

$$\text{FoM}(\theta) = [\det S(\theta)]^{-1/2}, \quad (29)$$

where $\det S(\theta)$ is the determinant of the parameter covariance. A larger FoM indicates tighter constraints.

4.3.3. Goodness of fit

We assess model goodness of fit using a posterior predictive distribution (PPD) test (Doux et al. 2021). This involves generating replicated data P^{rep} from the posterior and comparing the χ^2 statistic between replicated and observed data. The p -value is

$$p = \mathcal{P} \left[\chi^2(P^{\text{rep}}, \theta) > \chi^2(P^{\text{data}}, \theta) \mid P^{\text{data}} \right], \quad (30)$$

where the χ^2 has the same form as Eq. (26). Small p -values ($\lesssim 0.05$) indicate poor model fit, while very large ($\gtrsim 0.95$) ones may suggest covariance overestimation.

5. Baseline modelling choices for EFT and VDG_∞

In this section we investigate different modelling choices for the PT-based models, towards the definition of a baseline analysis configuration that will then be used in Sect. 6.1. This includes determining optimal nuisance parameters priors, scale cuts, and potentially fixing some of the tidal bias parameters to a given relation. For this exercise, we assume a covariance matrix corresponding to the full comoving volume of the mocks, in order to have the most stringent possible test.

5.1. Bias model assumptions

Figure 2 illustrates the relative performance of the EFT (red curves) and VDG_∞ (blue curves) model as a function of the maximum wave mode k_{max} for three different bias configurations:

- ‘maximal freedom’, where all bias parameters are allowed to vary freely (dashed lines with circle markers);
- ‘minimal freedom’, where both tidal biases γ_2 and γ_{21} are fixed to the excursion-set and co-evolution relations, respectively, as described in Sect. 3.1.5 (dotted lines with triangle markers);
- ‘intermediate’, where only the third-order tidal bias γ_{21} is fixed to the co-evolution relation (solid lines with diamond markers).

In the maximal-freedom case we observe that the inclusion of information from increasingly smaller scales impacts very differently the performance of the EFT and VDG_∞ models. In fact, the VDG_∞ model displays a significantly better p -value and FoB compared to the EFT model at high k_{max} , especially at lower redshifts, where the performance of the EFT model deteriorates substantially. Conversely, the VDG_∞ model exhibits a FoB that stays nearly flat across the explored redshift range – consistently staying within the 95% confidence interval except at $z = 0.9$ and $k_{\text{max}} = 0.4 \text{ h Mpc}^{-1}$ – while its constraining power displays a monotonic improvement. This trend is additionally reinforced by the p -value, which stabilises (around 0.5) once the fit starts including scales with higher signal-to-noise. On the other hand, for the EFT case the FoB exceeds the 2σ threshold at a typical scale of $k_{\text{max}} \sim 0.25\text{--}0.3 \text{ h Mpc}^{-1}$, pointing to a premature breaking of the model. On larger scales, at $k_{\text{max}} < 0.25 \text{ h Mpc}^{-1}$, the FoB and FoM of the two models are generally consistent to each other.

Compared to the maximal-freedom case, the use of the intermediate and minimal-freedom case results in neither EFT nor VDG_∞ showing any substantial improvement or degradation in terms of FoB and p -value across most redshift bins. However, when considering the VDG_∞ model, we notice a significant increase in the FoM, ranging from 50% to 100% improvement (as the k_{max} extends from 0.25 h Mpc^{-1} to about 0.4 h Mpc^{-1}), in a regime where both p -value and FoB are still within the 2σ threshold. On the other hand, the EFT model does not show a noticeable gain in the FoM when fixing only γ_{21} .

It is worth pointing out that recent full-shape analyses based on the EFT formalism use a maximum wave mode $k_{\text{max}} \lesssim 0.25 \text{ h Mpc}^{-1}$ (Ivanov et al. 2020; DESI Collaboration: Adame et al. 2025c), in agreement with the minimum scales where we find that no significant biases are introduced. Nonetheless, even in the maximal-freedom configuration, the maximally achievable FoM obtained with the VDG_∞ model (at $k_{\text{max}} \sim 0.35 \text{ h Mpc}^{-1}$) is about twice as large as the corresponding one obtained with the EFT model (at $k_{\text{max}} \sim 0.25 \text{ h Mpc}^{-1}$). Such improvement is more evident when assuming bias relations. For completeness, in Appendix B we add a detailed exploration on the parameter degeneracies exhibited by these two RSD models when assuming the bias relations previously discussed.

5.2. Test over different scale cuts per multipole

In the previous section, we adopted scale cuts where the maximum wave mode considered for the quadrupole and hexadecapole differ by $\Delta k = 0.05 \text{ h Mpc}^{-1}$ from the one of the monopole. In this section we provide a justification for this choice. Figure 3 presents the cosmology fits for three configurations with $\Delta k = (0, 0.05, 0.1) \text{ h Mpc}^{-1}$. For this analysis, we adopt the minimal-freedom bias model, which, as demonstrated in Fig. 2, gives a consistent performance to the maximal-freedom case in terms of FoB.

For the EFT model, the FoB shows a strong sensitivity to the amount of information contained in higher-order multipoles. Specifically, when using the same scale cut for all three multi-

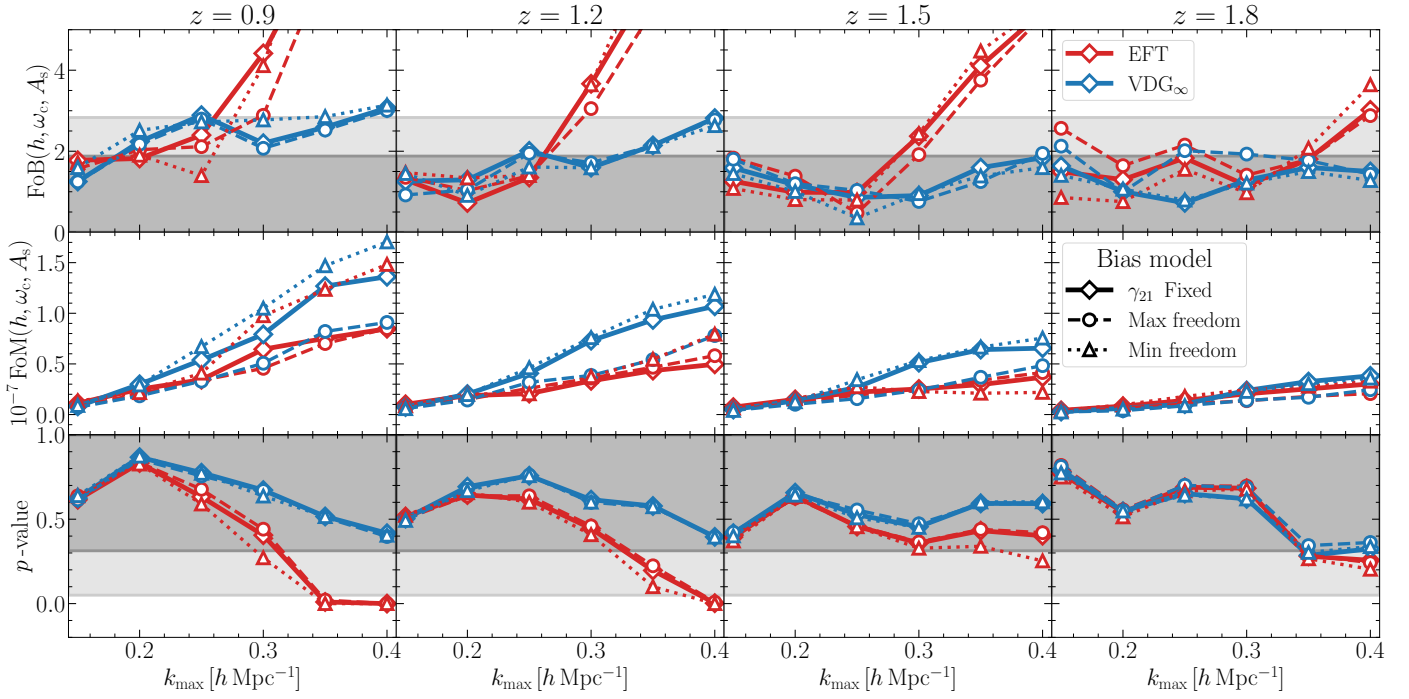


Fig. 2. Performance metrics – FoB, FoM, and p -value are shown in the *top*, *middle*, and *bottom row*, respectively – for the two different EPT models, here marked with different colours, as a function of the maximum fitting scale k_{\max} . For each case, we show the maximal-freedom configuration (dashed lines with circle markers), the minimal-freedom one (dotted lines with triangle markers), and the one with only γ_{21} fixed to the coevolution relation (solid lines with diamond markers). In all cases, we assume a covariance matrix matching the full volume of the Flagship comoving snapshots. *Each column* shows results at different redshift bins. The grey bands in the FoB and p -value panels represent the 68% and 95% percentiles of the corresponding distribution.

poles ($\Delta k = 0$), the model becomes biased already at $k_{\max} \sim 0.25 h \text{ Mpc}^{-1}$ for most redshifts, indicating a premature breaking of the RSD modelling on those scales. This trend is reflected in the goodness-of-fit, where the p -value consistently worsens when considering smaller scales in the quadrupole and hexadecapole. Despite the dependency of the FoM on Δk is weaker, it shows an improvement on scales where the model is still valid ($k_{\max} \leq 0.25 h \text{ Mpc}^{-1}$), particularly for the closest redshift. The combination of such trends indicates a slight preference for using $\Delta k = 0.10 h \text{ Mpc}^{-1}$.

In contrast, the VDG_{∞} model proves to be more robust against variations in Δk , showing no significant changes in terms of FoB or p -value. In this case, the FoM increases when incorporating additional information from higher-order multipoles, particularly at larger scales. Thus, the VDG_{∞} model slightly favours $\Delta k = 0 h \text{ Mpc}^{-1}$.

For our baseline RSD comparison, we set $\Delta k = 0.05 h \text{ Mpc}^{-1}$, as it represents a compromise of the Δk preferred by the two models. Finally, we verified that removing the hexadecapole from the fits only leads to marginal changes in the FoB and the FoM – indicating, particularly for the EFT case, that their behaviour is driven mainly by the quadrupole. Nonetheless, the p -value consistently deteriorates, due to a weaker constraint of nuisance parameters. Therefore, we choose to include the hexadecapole in our baseline comparison between the EFT and VDG_{∞} model. Further details on this comparison can be found in Appendix D.

5.3. Priors on noise and stochastic terms

In our main RSD model comparison, presented in Sect. 6.1, we fix γ_{21} to the co-evolution relation and neglect the anisotropic

noise contribution by setting $N_{22}^P = 0$. This specific configuration enables a more direct comparison between the EPT-based models and the hybrid approach.

On the contrary, in Fig. 4 we present the performance of both the EFT and VDG_{∞} models under different configurations of the shot-noise parameters. The circle markers and dashed lines correspond to the case where all noise terms are allowed to vary with uninformative priors. The solid lines show the baseline case that will be used in Sect. 6.1, for which $N_{22}^P = 0$. Removing the additional degree of freedom associated with the anisotropic noise does not significantly alter the performance of the models. However, setting both the scale-dependent and anisotropic noise contributions to zero, as shown by the dashed lines and triangle symbols, introduces an extra bias in the cosmological parameters. This bias is particularly pronounced for smaller scales and lower redshifts. For the EFT model, this configuration not only increases the FoB but also degrades the p -value. In Sect. 6.2.2 we discuss in more details the previous results.

5.4. Baseline setup for BACCO

In terms of the hybrid Lagrangian bias model, we use the BACCO code, specifically, the redshift-space hybrid bias emulator described in Pellejero Ibañez et al. (2023). This emulator has been tested on a variety of scenarios including HOD (Beyond-2pt Collaboration et al. 2025), SubHalo Abundance Matching (SHAM, Pellejero Ibañez et al. 2023), and observed data (Pellejero Ibañez et al. 2024).

For our specific analysis, we choose a k -binning for the data vectors much finer than the one used for the training of the original version of the BACCO emulator, which, convolved with the intrinsic noise in the training sample, leads to small but systematic

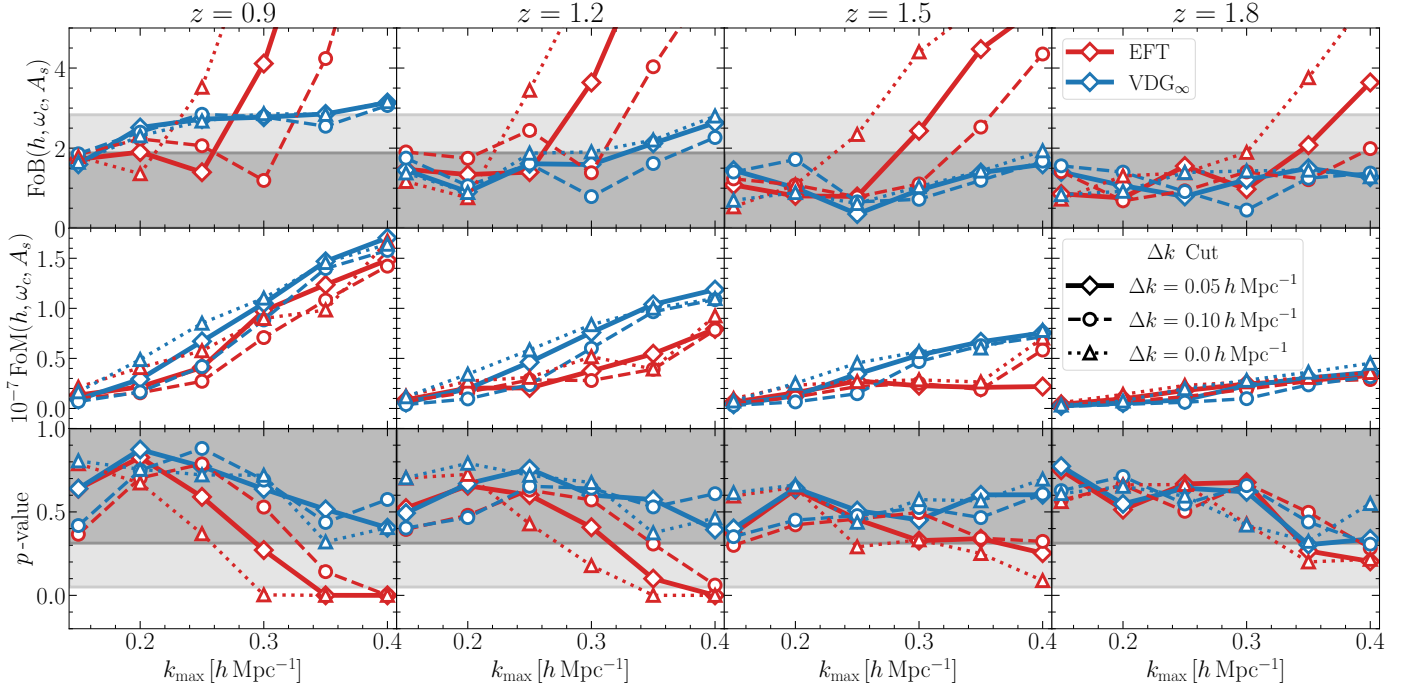


Fig. 3. Same as in Fig. 2, but only for the minimal-freedom bias configurations, and showing the impact of different values of Δk in the determination of the k_{\max} for the quadrupole and hexadecapole.

biases in the model predictions. Consequently, we use a different version of BACCO that was trained on a finer grid. A detailed explanation of this issue is added in Appendix A, where we also show how the current status of the BACCO code is not enough to deal with the Flagship I precision.⁹ Nonetheless, analysing a more realistic case such as the *Euclid*-like volume, is suitable to test the hybrid model. As a consequence, for our main results, we opt for comparing the three different RSD models only in the *Euclid*-like scenario.

While the current version of BACCO already enables robust applications in realistic survey settings, there is still room for improvement, and ongoing developments aim to extend its precision and applicability.

6. Results

In this section we summarise the main findings of our analysis for each of the RSD models introduced in Sect. 3. Our objective is to identify the smallest scale that can be adopted for each model configuration without introducing biases in the recovery of cosmological parameters, while still maximising the information extracted.

6.1. RSD model comparison

For this analysis we have rescaled the full volume of the Flagship I simulation to be closer to the *Euclid* survey, as defined in Sect. 2.3. Since the covariance has been rescaled, we focus our analysis in the FoB and FoM, not considering the goodness-of-fit. Instead of the p -value, we show the relative error on each cosmological parameter.

⁹ Alternatively, we could have chosen to re-bin the P_ℓ measurements, but since the errorbars shrinks accordingly with the increasing number of modes per bins, assuming the full Flagship volume still would have led to errorbars of the same order of the emulator precision.

In Fig. 5 we compare the three different RSD models described in Sect. 3 as a function of the maximum wave mode k_{\max} included in the fit. For the two EPT models, we only consider the intermediate configuration, with γ_{21} fixed to the co-evolution relation, and additionally set $N_{22}^P = 0$, in order to partially reproduce the same default configuration of the hybrid model from the BACCO emulator (see Sect. 3.2). The limits of the FoB are rescaled as described in Sec. 4.3.1, to make sure that they properly reflect the 68% and 95% FoB thresholds even after having rescaled the data covariance.

In terms of FoB, we observe that the three different RSD models are well behaved up to a maximum wave mode $k_{\max} = 0.25 h \text{ Mpc}^{-1}$, with deviations of at most $2\sigma_E$ for all the considered redshifts. Pushing the models to smaller scales, at $k_{\max} > 0.25 h \text{ Mpc}^{-1}$, the EFT model starts showing a worsening trend in the FoB compared to BACCO and the VDG_∞ models, particularly for the two closest redshifts, where the FoB crosses the $2\sigma_E$ threshold immediately above $k_{\max} = 0.25 h \text{ Mpc}^{-1}$. For the snapshots at $z = 1.5$ and $z = 1.8$, the crossing of the $2\sigma_E$ threshold occurs at slightly larger wave modes, namely at $k_{\max} = 0.35 h \text{ Mpc}^{-1}$ and $k_{\max} = 0.4 h \text{ Mpc}^{-1}$, respectively, due to the more linear behaviour at high z . Nonetheless, a growing trend in the FoB can still be observed starting from $k_{\max} \gtrsim 0.25 h \text{ Mpc}^{-1}$. On the other hand, for most of the redshifts and scales explored in this work, both the VDG_∞ and BACCO models return a FoB of at most $2\sigma_E$, without any clear indication for a growing trend in the FoB.

In terms of FoM, BACCO consistently displays slightly better constraining power on scales $k_{\max} \lesssim 0.20 h \text{ Mpc}^{-1}$, compared to the EFT and VDG_∞ models. However we notice that over these scales some of the nuisance parameters of BACCO hit their prior boundaries, potentially affecting the marginalised pos-

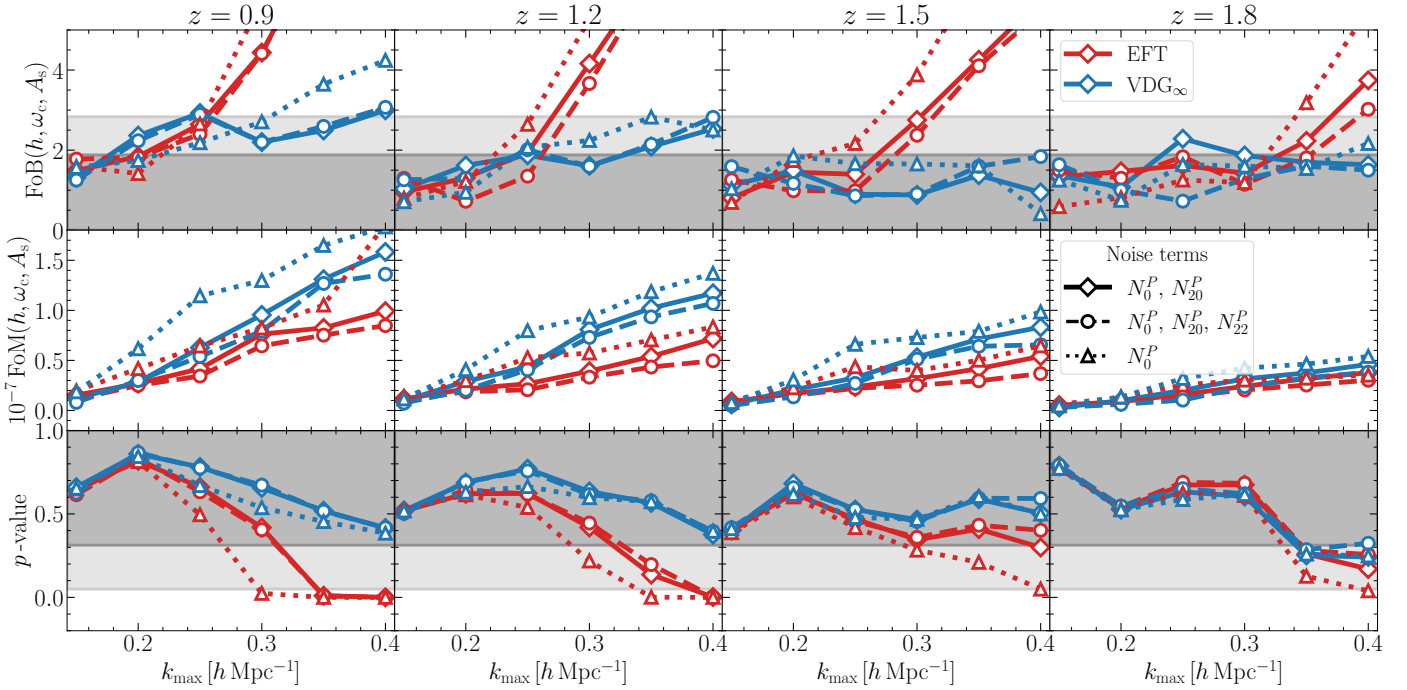


Fig. 4. Same as in Fig. 2, but only for the minimal-freedom bias configurations, and showing the impact of different configurations for the shot-noise parameters.

terior distribution of the cosmological parameters.¹⁰ It is also worth noticing that, across all redshifts, the gain in constraining power for both BACCO and the VDG_∞ model roughly doubles when comparing the FoM at $k_{\max} \simeq 0.40 h \text{ Mpc}^{-1}$ to the one at $k_{\max} = 0.25 h \text{ Mpc}^{-1}$ – beyond the range of validity of the EFT model. The flattening behaviour displayed by BACCO at $z = 1.8$ (also present, though less prominent, at the other redshifts) and $k_{\max} > 0.3 h \text{ Mpc}^{-1}$, can be interpreted as a saturation of the information that can be extracted on these scales. In contrast, the VDG_∞ model benefits from smaller-scale information to better constrain cosmological parameters, keeping a stable growing trend up to the minimum scale explored in this work.

The third row in Fig. 5 shows the constraining power on each of the cosmological parameters considered. This panel allows us to identify which parameters are better constrained in our fits. In particular, we notice that h can be recovered with a precision of 1% by all models, despite reaching a plateau in the information content when pushing the model to smaller scales. The matter density parameter ω_c is recovered at the 3% level. Additionally, only with the VDG_∞ model, it is possible to achieve a precision better than 5% on A_s without introducing any significant bias. Finally, in the case of BACCO, we note that ω_c is already well constrained from the first k -bin. However, its precision improvement is minimal when smaller scales are included in the analysis. Further, after $k_{\max} \gtrsim 0.25 h \text{ Mpc}^{-1}$ it follows the same trend as in VDG_∞ and EFT. Such trend suggests that if affected by prior boundaries, the impact is only significant for the first k -bin.

In Fig. 6 we show the evolution as a function of k_{\max} of the marginalised 1-dimensional posterior distribution for each one of the cosmological parameters. The shaded regions correspond to their 68% confidence interval, centred at their mean marginalised posterior value, whereas star symbols correspond

to the maximum-likelihood position as estimated from the collected samples. The different colours correspond to different RSD models, as indicated in the legend. We find that the fiducial values of the three cosmological parameters are recovered within the 1σ region for most of the scale cuts both when using BACCO and the VDG_∞ model, with the only exception at $z = 1.8$, where BACCO displays a bias in h beyond $k_{\max} = 0.20 h \text{ Mpc}^{-1}$. Otherwise, we observe that for the EFT model, particularly at the two closest redshifts, the parameters responsible for returning a larger FoB are h and A_s .

Some recent works (Holm et al. 2023; Carrilho et al. 2023) have shown that in state-of-art models (including several nuisance parameters per spectroscopic bin), the marginalised posterior parameter distributions is subject to strong prior-volume effects. Nonetheless, in a sample covering a large enough volume, as it is our case, this effect is negligible due to a more Gaussian likelihood (Holm et al. 2023).¹¹ For completeness, in Fig. 6 we inspect the location of the maximum-likelihood values, finding that in the vast majority of cases explored in this work, it traces the mean of the posterior distribution, lying well within the 1σ marginalised contours. This result is in agreement with previous works, finding negligible prior-volume effects for the standard Λ CDM cosmology but becoming significant for extended cosmologies (DESI Collaboration: Adame et al. 2025a; Carrilho et al. 2023; Moretti et al. 2023).

6.2. Posteriors of nuisance parameters for the EPT models

In this section we focus on the two EPT models and compare them at the level of the nuisance parameters, precisely focusing on those that regulate the amplitude of RSD and UV effects plus those controlling the stochastic corrections. For this test we adopt the most stringent error bars – corresponding to the full

¹⁰ In Appendix E we describe some tests of the differences in the perturbative treatment and priors implemented in BACCO, compared to VDG_∞ and EFT, finding that priors could lead to extra gains at larger scales.

¹¹ In Appendix F we test that more restrictive priors for the Flagship covariance case do not change our main conclusions.

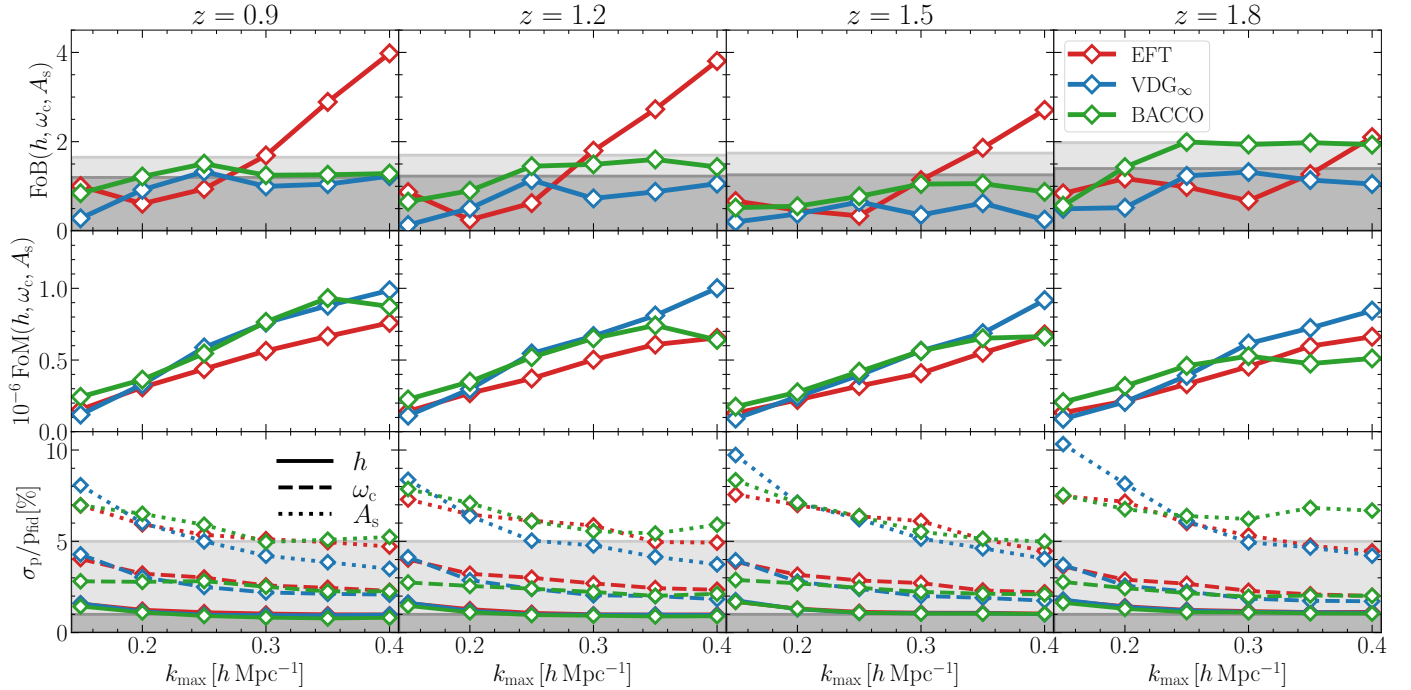


Fig. 5. Performance metrics for the three RSD models presented in Sect. 3 assuming a covariance matrix matching the expected volume by the end of the *Euclid* mission. The FoB and FoM are shown in the first two columns, while the bottom panel shows the relative error of each parameter with respect to its fiducial value, as indicated in the legend. Each column shows results for a different redshift bin. Different colours correspond to different models, as described in the legend. To have a consistent number of degrees of freedom, for the EFT-based models, we adopt the configuration with γ_{21} fixed to the co-evolution relation and the anisotropic noise contribution N_{22}^P set to 0. The x axis shows the maximum wave mode k_{\max} adopted in the fit. The grey bands in the FoB panel represent the 68% and 95% percentiles of the corresponding FoB distribution, as explained in Sect. 4.3.1.

Flagship I volume – to better identify differences between the two models.

6.2.1. Running of the counterterms

As explained in Sect. 3, the counterterms play distinct roles in the two EPT-based models. In the EFT framework, these are mostly meant to capture the small-scale real- to redshift-space mapping, while additionally describing extra contributions coming from higher derivatives, halo exclusion, and velocity bias. On the other hand, in the VDG_∞ model, the small-scale redshift-space mapping is captured by the analytical damping function W_∞ , leaving to the counterterms the role of describing effects other than RSD. In Fig. 7 we explore the behaviour of the counterterms at $k_{\max} > 0.25 h \text{ Mpc}^{-1}$ for the two closest redshift snapshots. Our goal is mostly to understand the behaviour of the counterterms in these configurations of the EFT model, where it becomes progressively more biased than the VDG_∞ model, as indicated in Fig. 5.

The first noticeable trend is that on scales $k_{\max} \geq 0.25 h \text{ Mpc}^{-1}$ the 2-dimensional posteriors of the EFT model exhibit a drift in the c_2-c_4 plane. This indicates that these parameters start absorbing residual effects at the expense of their main physical motivation. In contrast, the posteriors of the VDG_∞ model converge to well localised positions, suggesting that these constraints benefit from the additional information carried by more nonlinear scales without introducing systematic biases. The second trend is related to the position at which the 2-dimensional c_2-c_0 constraints converge. For the EFT model, this position deviates significantly from zero, which is expected due to the role of the counterterms of modelling the small-scale RSD

effect. On the other hand, in the VDG_∞ model, these parameters display a smooth convergence towards zero, particularly c_0 , in a consistent way to results obtained in real-space.¹² This behaviour indicates that the damping function in the VDG_∞ model is efficient in reproducing the impact from RSD on small-scales, leaving mainly residual effects to be absorbed by counterterms.

6.2.2. Constraints on stochasticity

The results from the different shot-noise configurations observed in Sect. 5.3 can be better understood by inspection of the individual marginalised posterior of the shot-noise parameters. This is shown in Fig. 8, where we present marginalised 2-dimensional constraints of the parameters $(N_0^P, N_{20}^P, N_{22}^P)$. Although here we focus on the maximal-freedom case, the same conclusions hold when γ_{21} is fixed to the co-evolution relation. Similarly to the tests from Sect. 6.2.1, we explore scale cuts limited at $k_{\max} \geq 0.25 h \text{ Mpc}^{-1}$ and at the two closest redshifts, aiming to better understand whether such parameters compensate modelling failures.

We find that, while in the EFT model the constant deviation from purely Poissonian noise, N_0^P , is recovered only at the 2σ level, in the VDG_∞ model it is consistently constrained at the 1σ level. This may be one of the factors contributing to the enhanced constraining power of VDG_∞ , given its degeneracy with b_1 and A_s . As shown in Fig. 5, A_s is precisely the parameter for which VDG_∞ provides significantly tighter constraints compared to EFT.

¹² See Fig. F1 in [Euclid Collaboration: Pezzotta et al. \(2024\)](#) for the corresponding real-space analysis.

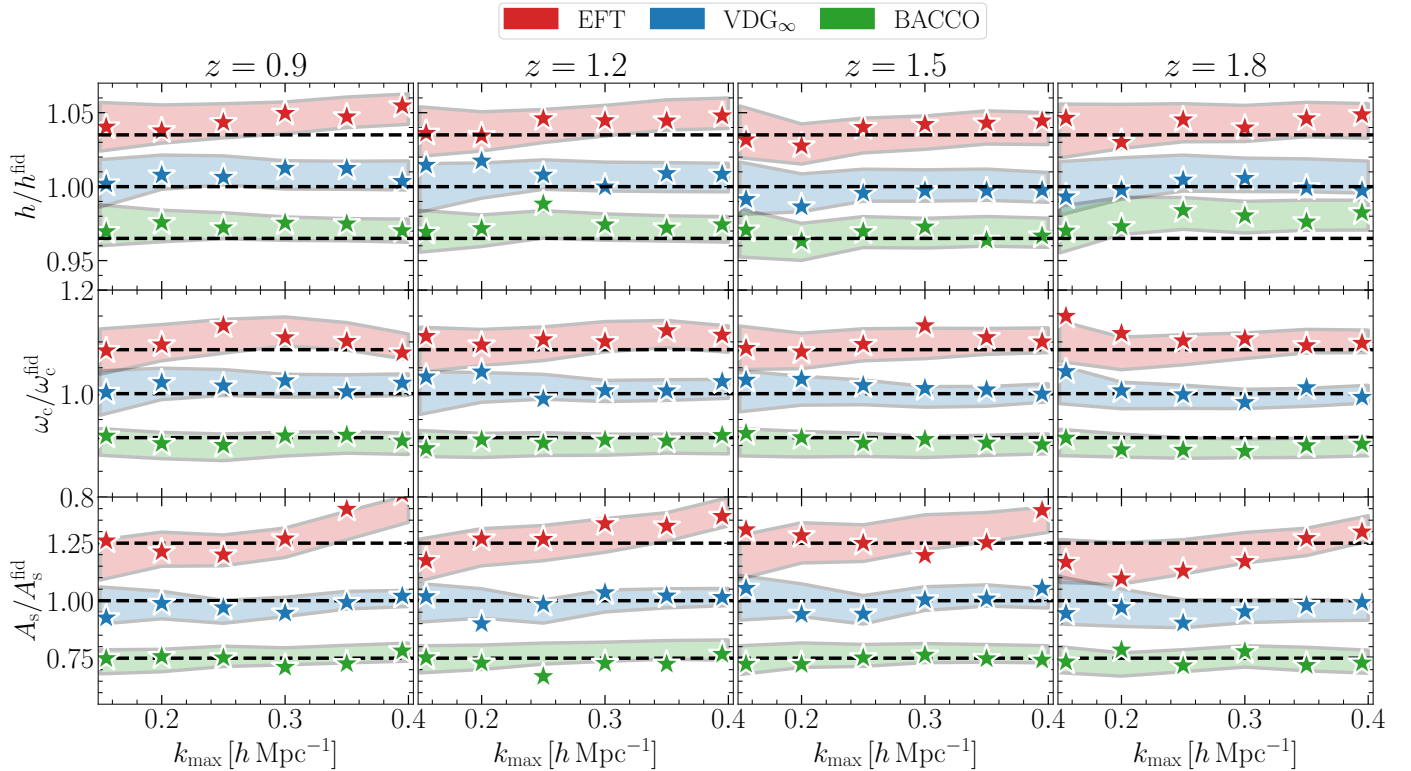


Fig. 6. Evolution of the marginalised 1-dimensional posterior of each cosmological parameter, where shaded areas represent the 68% confidence interval, centred around the mean values, of the posterior distribution normalised by the corresponding fiducial value. The normalised maximum-likelihood parameters, estimated by considering the position with the highest likelihood value obtained during the sampling process, are denoted with star symbols. The three cosmological parameters are shown in *each one of the rows*, while the *columns* display different redshifts. The colours correspond to the three RSD models, as indicated in the legend. The dashed lines show the fiducial position for each of the cosmological parameters. For visualisation purposes, we have shifted the expected ratios by a constant value for each of the RSD models, so that the different areas do not overlap.

The second important observation is that, while the EFT model recovers a non-zero scale-dependent noise term ($N_{20}^P \neq 0$), for VDG_∞ this term is generally consistent with zero. This behaviour better aligns with findings from real-space analyses (see Fig. 8 in [Euclid Collaboration: Pezzotta et al. 2024](#)).

Lastly, both models show that the anisotropic stochastic term N_{22}^P is generally consistent with zero, though the EFT model at $z = 1.2$ displays a mild deviation from zero. Although the real values of these parameters depend on the specific galaxy sample under consideration, the constraints of N_0^P suggest that VDG_∞ performs better than EFT in capturing the amplitude of the shot-noise corrections.

6.2.3. Next-to-leading order effects

In the EFT model, higher-order corrections that are not fully reproduced by the leading-order expansion of the moment generating function are captured through the next-to-leading order parameter c_{nlo} . In the VDG_∞ model this parameter is not necessary, since the exponential prefactor is modelled analytically as described in Eq. (8). The large-scale limit of the VDG includes an extra degree of freedom represented by the parameter a_{vir} , which is meant to reproduce the kurtosis of the pairwise velocity difference distribution.

In Fig. 9 we show the 2-dimensional marginalised posterior distribution of c_{nlo} and a_{vir} against the three cosmological parameters (A_s, h, ω_c). Consistently with the approach adopted in Sects. 6.2.1 and 5.3, we explore scale cuts with $k_{\max} \geq$

$0.25 h \text{ Mpc}^{-1}$ for the two closest redshifts. In this case, we observe a notable drift in the posteriors of c_{nlo} , which is significantly correlated to shifts in the scalar amplitude A_s . This behaviour suggests that, similarly to the lower-order counterterms, c_{nlo} absorbs residual effects beyond its physical motivation. On the other hand, the a_{vir} parameter exhibits a stable trend as a function of k_{\max} , with no significant degeneracy with any cosmological parameter.

7. Conclusions

In this work, we compared different modelling prescriptions for the galaxy power spectrum in redshift space. Specifically, we tested the performance of three different redshift-space models: BACCO, EFT, and VDG_∞ . To test their performance, we made use of a set of synthetic samples of $H\alpha$ -emitting galaxies, populated in comoving snapshots of the Flagship I simulation and tailored to reproduce the clustering properties of the main spectroscopic sample that will be collected by *Euclid*. The relative quality of the different models was assessed by means of three performance metrics: the FoM, the FoB, and the p -value, to quantify constraining power, accuracy, and goodness-of-fit, respectively. While the assumed HOD for building the catalogues may impact the performance of the different theoretical approaches ([Findlay et al. 2025](#)), the errors associated to the assumed HOD are currently under investigation in Euclid Collaboration: Gambardella et al. (in prep.).

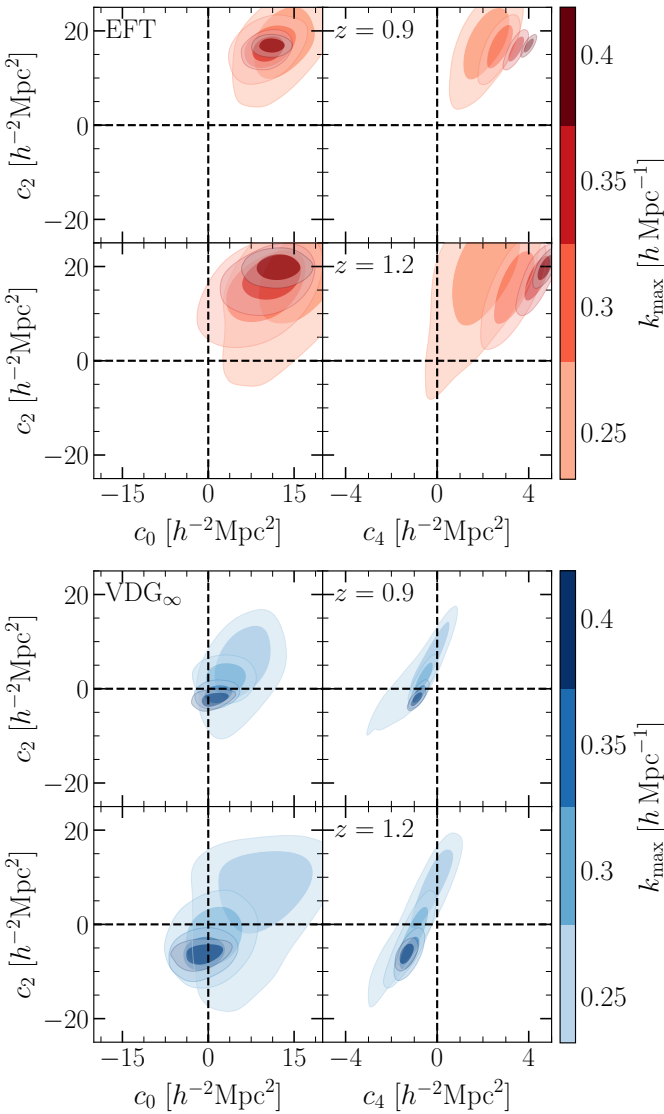


Fig. 7. 2-dimensional posterior distribution of the leading-order counterterms (c_0 , c_2 , c_4) for both the EPT-based models. The *top and bottom set of panels* corresponds to the EFT and VDG_∞ model, respectively. In both sets, the *first and second row* corresponds to the $z = 0.9$ and $z = 1.2$ snapshot, respectively. Dashed lines indicate the zero value.

The main conclusion from the comparison among the three different models is that, for all the metrics, VDG_∞ and BACCO exhibit a consistent behaviour across most of the considered redshifts and scale cuts. However, at the highest redshifts, the VDG_∞ model benefits the most from the information contained on smaller scales. In contrast, the EFT model shows an increasing trend in the FoB at $k_{\max} \geq 0.25 h \text{ Mpc}^{-1}$ – eventually leaving the 2σ region – which is further associated with a smaller ($\sim 20\%$) FoM compared to VDG_∞ and BACCO.

In detail, in terms of FoM, in the baseline analysis (where both EPT models fix γ_{21} and $N_{22}^P = 0$) BACCO consistently delivers a larger constraining power on cosmological parameters at $k_{\max} \lesssim 0.25 h \text{ Mpc}^{-1}$ compared to EFT and VDG_∞ . Moreover, the amount of information that can be extracted saturates at a typical scale of $k_{\max} \approx 0.35 h \text{ Mpc}^{-1}$. On the contrary, the VDG_∞ model benefits more of the additional signal at $k_{\max} \geq 0.35 h \text{ Mpc}^{-1}$, displaying a monotonically increasing FoM over the whole range of scales considered. In terms

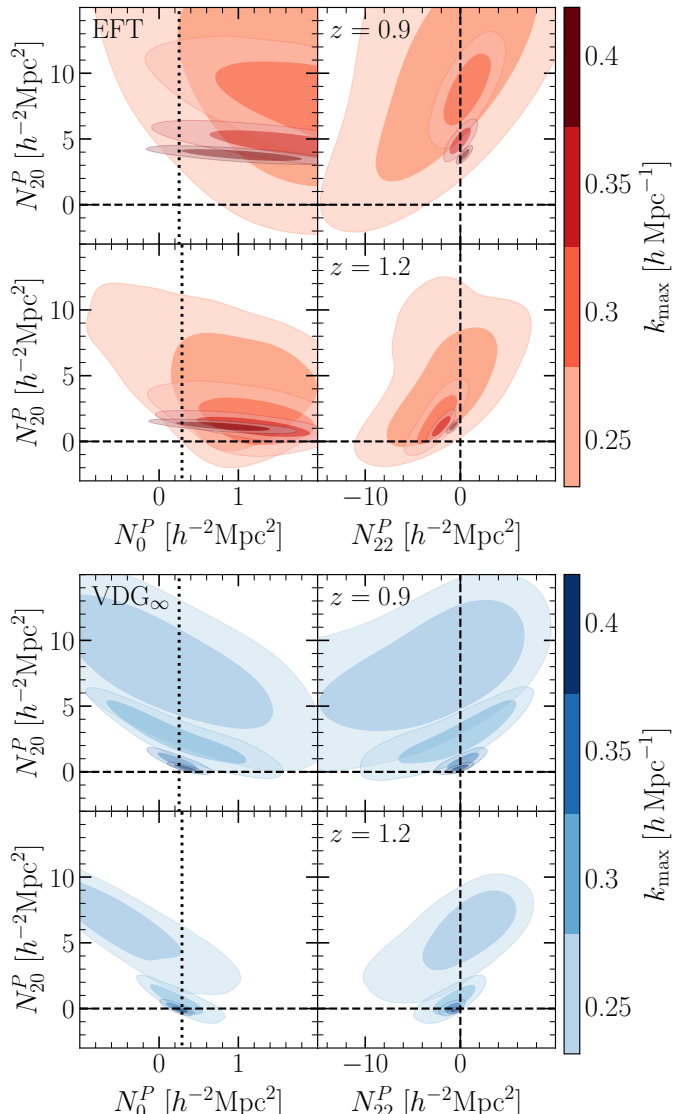


Fig. 8. 2-dimensional posterior distribution of the shot-noise parameters (N_0^P , N_{20}^P , N_{22}^P) for both EPT models. The *top and bottom set of panels* corresponds to the EFT and VDG_∞ models, respectively. In both sets, the *first and second row* corresponds to the $z = 0.9$ and $z = 1.2$ snapshot, respectively. Dotted lines in N_0^P show the large-scale value recovered from linear-theory fits of the $P_{\text{gg}}/P_{\text{mm}}$ ratio. Otherwise, for N_{20}^P and N_{22}^P , dashed lines indicate the zero value.

of FoB, BACCO and VDG_∞ hold inside the 1σ and 2σ region, respectively, when including more nonlinear information coming from smaller scales. Conversely, the EFT model shows a growing trend of the FoB at smaller scales, particularly for the two closest redshifts, suggesting a range of validity that stops at $k_{\max} \approx 0.25 h \text{ Mpc}^{-1}$, in agreement with previous works. We further examined the constraints on individual cosmological parameters. The Hubble parameter h is recovered with 1% accuracy for all models. The parameter ω_c is recovered within 3% accuracy, with BACCO and VDG_∞ showing similar precision. VDG_∞ outperforms BACCO and EFT in constraining A_s , achieving better than 5% precision at all redshifts when including the smallest considered scales.

While validating our bias assumptions and assessing potential failures of the EPT models, we found that the inclusion of higher multipoles in the fit (our baseline setup) generally im-

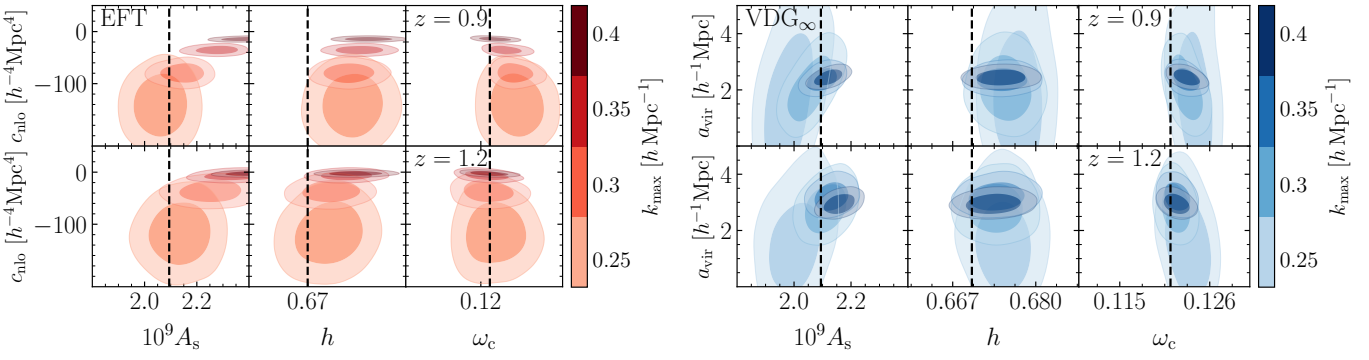


Fig. 9. 2-dimensional posterior distribution of the cosmological parameters (A_s , h , ω_c), the next-to-leading order parameter c_{nlo} of the EFT model, and the parameter a_{vir} of the VDG_∞ model. The *left- and right-hand side panels* correspond to the EFT and VDG_∞ model posteriors, respectively. In each panel, the *first and second row* corresponds to the $z = 0.9$ and $z = 1.2$ snapshots, respectively.

proves the constraining power (few percent) of the VDG_∞ model without introducing significant biases. However, with the EFT model, the additional modelling of the quadrupole and hexadecapole leads to an increasing bias – leaving the 2σ region at $k_{\text{max}} > 0.20 h \text{ Mpc}^{-1}$ – and a worse goodness-of-fit at smaller scales – leaving the 2σ region at $k_{\text{max}} \geq 0.30 h \text{ Mpc}^{-1}$ for the closest redshift. In terms of stochastic contributions, we observed a k^2 -dependent factor, generally necessary in both models to avoid the presence of bias on the recovered cosmological parameters. Nevertheless, neglecting such term affects VDG_∞ only at the smallest scales of the closest redshift bins, while enhancing its constraining power.

Counterterms are an essential ingredient in EFT to account for nonlinearities and RSD at smaller scales. However, the impact of these terms seems to be limited. First, it can be seen that EFT already increases its FoB beyond the 2σ region at $k_{\text{max}} \gtrsim 0.25 h \text{ Mpc}^{-1}$. Moreover, the amplitude of c_0 , c_2 , and c_4 – in general – departs significantly from unity (on the order of tens, not expected for a perturbative approach). Otherwise, in the VDG_∞ case, the corrections introduced by counterterms seem, in general, smaller, with c_0 generally compatible with zero. Additionally, higher-order corrections, encapsulated in the damping function in VDG_∞ , are crucial for maintaining accuracy at smaller scales, ensuring robust performance with minimal biases (not going beyond the 2σ region). On the other hand, EFT's higher-order corrections are encapsulated in c_{nlo} , which is poorly constrained at intermediate scales.

In summary, our baseline analysis clarifies both the strengths and limitations of BACCO, EFT, and VDG_∞ for modelling the anisotropic power spectrum. Our results show that the choice of model and the adopted scale range play a central role in optimising parameter constraints. In particular, improved mappings from real to redshift space, as implemented in VDG_∞ and BACCO, substantially extend the range of validity of the theoretical predictions up to $k_{\text{max}} \approx 0.40 h \text{ Mpc}^{-1}$. While BACCO enables accurate analyses over a broad range of nonlinear scales, this comes at the cost of significantly higher computational demands compared to EFT and VDG_∞ . Otherwise, although models such as EFT still require refinement to reach smaller scales, their fully theory-driven construction provides more flexibility when exploring modified gravity or alternative dark energy scenarios. Finally, we find that counterterms and higher-order corrections are essential for achieving accurate predictions; although stabilising them remains challenging, ongoing efforts toward physically motivated priors are a promising path forward. All these developments are essential for building increasingly precise and

reliable theoretical frameworks for upcoming large-scale structure surveys.

Acknowledgements. The Euclid Consortium acknowledges the European Space Agency and a number of agencies and institutes that have supported the development of *Euclid*, in particular the Agenzia Spaziale Italiana, the Austrian Forschungsförderungsgesellschaft funded through BMIMI, the Belgian Science Policy, the Canadian Euclid Consortium, the Deutsches Zentrum für Luft- und Raumfahrt, the DTU Space and the Niels Bohr Institute in Denmark, the French Centre National d'Etudes Spatiales, the Fundação para a Ciência e a Tecnologia, the Hungarian Academy of Sciences, the Ministerio de Ciencia, Innovación y Universidades, the National Aeronautics and Space Administration, the National Astronomical Observatory of Japan, the Nederlandse Onderzoekschool Voor Astronomie, the Norwegian Space Agency, the Research Council of Finland, the Romanian Space Agency, the State Secretariat for Education, Research, and Innovation (SERI) at the Swiss Space Office (SSO), and the United Kingdom Space Agency. A complete and detailed list is available on the *Euclid* web site (www.euclid-ec.org/consortium/community/). The majority of the analysis carried out in this manuscript has been produced by a joint effort among several Euclid members and work centers. A special acknowledgement goes to the Max Planck Computing and Data Facility (MPCDF) in Garching, where most of the presented results have been obtained. This research made use of matplotlib, a Python library for publication quality graphics (Hunter 2007).

References

Abbott, T. M. C., Aguena, M., Alarcon, A., et al. 2022, Phys. Rev. D, 105, 023520
 Alam, S., Aubert, M., Avila, S., et al. 2021, Phys. Rev. D, 103, 083533
 Angulo, R. E. & White, S. D. M. 2010, MNRAS, 405, 143
 Angulo, R. E., Zennaro, M., Contreras, S., et al. 2021, MNRAS, 507, 5869
 Aricò, G., Angulo, R. E., & Zennaro, M. 2022, Open Research Europe, 1, 152
 Baldauf, T., Mirbabayi, M., Simonović, M., & Zaldarriaga, M. 2015, Phys. Rev. D, 92, 043514
 Ballinger, W. E., Peacock, J. A., & Heavens, A. F. 1996, MNRAS, 282, 877
 Bernardeau, F., Colombi, S., Gaztañaga, E., & Scoccimarro, R. 2002, Phys. Rep., 367, 1
 Beutler, F., Blake, C., Colless, M., et al. 2012, MNRAS, 423, 3430
 Beutler, F., Seo, H.-J., Ross, A. J., et al. 2016, MNRAS, 464, 3409
 Beyond-2pt Collaboration, Krause, E., Kobayashi, Y., et al. 2025, ApJ, 990, 99
 Blake, C., Brough, S., Colless, M., et al. 2011, MNRAS, 415, 2876
 Blas, D., Garny, M., Ivanov, M. M., & Sibiryakov, S. 2016, JCAP, 07, 028
 Blot, L., Crocce, M., Sefusatti, E., et al. 2019, MNRAS, 485, 2806
 Brout, D., Scolnic, D., Popovic, B., et al. 2022, ApJ, 938, 110
 Carrasco, J. J. M., Hertzberg, M. P., & Senatore, L. 2012, J. High Energy Phys., 09, 82
 Carrilho, P., Moretti, C., & Poutsidou, A. 2023, JCAP, 01, 028
 Carrilho, P., Moretti, C., & Tsedrik, M. 2023, arXiv:2310.07344
 Chan, K. C., Scoccimarro, R., & Sheth, R. K. 2012, Phys. Rev. D, 85, 083509
 Chen, S.-F., Vlah, Z., & White, M. 2020, JCAP, 07, 062
 Coles, P. 1993, MNRAS, 262, 1065
 Colless, M., Dalton, G., Maddox, S., et al. 2001, MNRAS, 328, 1039
 Crocce, M. & Scoccimarro, R. 2006, Phys. Rev. D, 73, 063520
 Crocce, M. & Scoccimarro, R. 2008, Phys. Rev. D, 77, 023533
 d'Amico, G., Gleyzes, J., Kokron, N., et al. 2020, JCAP, 05, 005

Dark Energy Survey and Kilo-Degree Survey Collaboration, Abbott, T. M. C., Aguena, M., et al. 2023, *The Open Journal of Astrophysics*, 6, 36

Dawson, K. S., Kneib, J.-P., Percival, W. J., et al. 2016, *AJ*, 151, 44

Dawson, K. S., Schlegel, D. J., Ahn, C. P., et al. 2012, *AJ*, 145, 10

Dekel, A. & Lahav, O. 1999, *ApJ*, 520, 24

DES Collaboration: Abbott, T. M. C., Aguena, M., Alarcon, A., et al. 2025, *Phys. Rev. D*, 112, 083535

DESI Collaboration: Abdul Karim, M., Aguilar, J., Ahlen, S., et al. 2025, *Phys. Rev. D*, 112, 083515

DESI Collaboration: Adame, A. G., Aguilar, J., Ahlen, S., et al. 2025a, *JCAP*, 07, 028

DESI Collaboration: Adame, A. G., Aguilar, J., Ahlen, S., et al. 2025b, *JCAP*, 02, 021

DESI Collaboration: Adame, A. G., Aguilar, J., Ahlen, S., et al. 2025c, *JCAP*, 09, 008

DESI Collaboration: Aghamousa, A., Aguilar, J., Ahlen, S., et al. 2016, *arXiv:1611.00036*

Desjacques, V., Crocce, M., Scoccimarro, R., & Sheth, R. K. 2010, *Phys. Rev. D*, 82, 103529

Desjacques, V., Jeong, D., & Schmidt, F. 2018a, *Phys. Rep.*, 733, 1

Desjacques, V., Jeong, D., & Schmidt, F. 2018b, *JCAP*, 12, 035

Doux, C., Baxter, E., Lemos, P., et al. 2021, *MNRAS*, 503, 2688

Driver, S. P., Hill, D. T., Kelvin, L. S., et al. 2011, *MNRAS*, 413, 971

Eggemeier, A., Camacho-Quevedo, B., Pezzotta, A., et al. 2023, *MNRAS*, 519, 2962

Eggemeier, A., Lee, N., Scoccimarro, R., et al. 2025, *Phys. Rev. D*, 112, 063532

Eggemeier, A., Scoccimarro, R., Crocce, M., Pezzotta, A., & Sánchez, A. G. 2020, *Phys. Rev. D*, 102, 103530

Eggemeier, A., Scoccimarro, R., & Smith, R. E. 2019, *Phys. Rev. D*, 99, 123514

Eggemeier, A., Scoccimarro, R., Smith, R. E., et al. 2021, *Phys. Rev. D*, 103, 123550

Eisenstein, D. J., Seo, H.-J., & White, M. 2007, *ApJ*, 664, 660

Eisenstein, D. J., Zehavi, I., Hogg, D. W., et al. 2005, *ApJ*, 633, 560

Euclid Collaboration: Blanchard, A., Camera, S., Carbone, C., et al. 2020, *A&A*, 642, A191

Euclid Collaboration: Castander, F. J., Fosalba, P., Stadel, J., et al. 2025, *A&A*, 697, A5

Euclid Collaboration: Guidi, M., Veropalumbo, A., Pugno, A., et al. 2025, *A&A*, submitted, *arXiv:2506.22257*

Euclid Collaboration: Kärcher, M., Breton, M.-A., de la Torre, S., et al. 2026, *A&A*, submitted, *arXiv:2601.04780*

Euclid Collaboration: Mellier, Y., Abdurro'uf, Acevedo Barroso, J. A., et al. 2025, *A&A*, 697, A1

Euclid Collaboration: Monaco, P., Elkhashab, M. Y., Granett, B. R., et al. 2025, *A&A*, submitted, *arXiv:2511.20856*

Euclid Collaboration: Pezzotta, A., Moretti, C., Zennaro, M., et al. 2024, *A&A*, 687, A216

Findlay, N., Nadathur, S., Percival, W. J., et al. 2025, *JCAP*, 09, 007

Fisher, K. B. 1995, *ApJ*, 448, 494

Frusciante, N. & Sheth, R. K. 2012, *JCAP*, 11, 016

Fry, J. N. 1996, *ApJ*, 461, L65

Fry, J. N. & Gaztanaga, E. 1993, *ApJ*, 413, 447

Grieb, J. N., Sánchez, A. G., Salazar-Albornoz, S., & Dalla Vecchia, C. 2016, *MNRAS*, 457, 1577

Guzzo, L., Scoggio, M., Garilli, B., et al. 2014, *A&A*, 566, A108

Hamilton, A. J. S. 1992, *ApJ*, 385, L5

Hinshaw, G., Larson, D., Komatsu, E., et al. 2013, *ApJ*, 208, 19

Holm, E. B., Herold, L., Simon, T., et al. 2023, *Phys. Rev. D*, 108, 123514

Hunter, J. D. 2007, *Computing in Science & Engineering*, 9, 90

Ivanov, M. M. & Sibiryakov, S. 2018, *JCAP*, 07, 053

Ivanov, M. M., Simonović, M., & Zaldarriaga, M. 2020, *JCAP*, 05, 042

Kaiser, N. 1987, *MNRAS*, 227, 1

Kokron, N., DeRose, J., Chen, S.-F., White, M., & Wechsler, R. H. 2021, *MNRAS*, 505, 1422

Laureijs, R., Amiaux, J., Arduini, S., et al. 2011, *arXiv:1110.3193*

Le Fèvre, Cassata, P., Cucciati, O., et al. 2013, *A&A*, 559, A14

Lewis, A. 2025, *JCAP*, 08, 025

Li, S.-S., Hoekstra, H., Kuijken, K., et al. 2023, *A&A*, 679, A133

Louis, T., La Posta, A., Atkins, Z., et al. 2025, *arXiv:2503.14452*

Manera, M., Sheth, R. K., & Scoccimarro, R. 2010, *MNRAS*, 402, 589

Matsubara, T. 1999, *ApJ*, 525, 543

Matsubara, T. 2008, *Phys. Rev. D*, 77, 063530

Modi, C., Chen, S.-F., & White, M. 2020, *MNRAS*, 492, 5754

Moretti, C., Tsedrik, M., Carrilho, P., & Poursidou, A. 2023, *JCAP*, 12, 025

Orsi, Á. A. & Angulo, R. E. 2018, *MNRAS*, 475, 2530

Peacock, J. A., Cole, S., Norberg, P., et al. 2001, *Nat*, 410, 169

Pellejero Ibañez, M., Angulo, R. E., Jamieson, D., & Li, Y. 2024, *MNRAS*, 529, 89

Pellejero Ibañez, M., Angulo, R. E., & Peacock, J. A. 2024, *MNRAS*, 534, 3595

Pellejero Ibañez, M., Angulo, R. E., Zennaro, M., et al. 2023, *MNRAS*, 520, 3725

Pellejero Ibañez, M., Stückler, J., Angulo, R. E., et al. 2022, *MNRAS*, 514, 3993

Perko, A., Senatore, L., Jennings, E., & Wechsler, R. H. 2016, *arXiv:1610.09321*

Pezzotta, A., Crocce, M., Eggemeier, A., Sánchez, A. G., & Scoccimarro, R. 2021, *Phys. Rev. D*, 104, 043531

Pezzotta, A., Eggemeier, A., Gambardella, G., et al. 2025, *Phys. Rev. D*, 112, 023520

Philcox, O. H. E. & Ivanov, M. M. 2022, *Phys. Rev. D*, 105, 043517

Planck Collaboration, Aghanim, N., Akrami, Y., et al. 2020, *A&A*, 641, A6

Potter, D., Stadel, J., & Teyssier, R. 2017, *Computational Astrophysics and Cosmology*, 4, 2

Pozzetti, L., Hirata, C. M., Geach, J. E., et al. 2016, *A&A*, 590, A3

Pueblas, S. & Scoccimarro, R. 2009, *Phys. Rev. D*, 80, 043504

Sánchez, A. G., Montesano, F., Kazin, E. A., et al. 2014, *MNRAS*, 440, 2692

Sánchez, A. G., Scoccimarro, R., Crocce, M., et al. 2016, *MNRAS*, 464, 1640

Schmidt, F., Jeong, D., & Desjacques, V. 2013, *Phys. Rev. D*, 88, 023515

Scoccimarro, R. 2004, *Phys. Rev. D*, 70, 083007

Scoccimarro, R., Couchman, H. M. P., & Frieman, J. A. 1999, *ApJ*, 517, 531

Scoccimarro, R., Sefusatti, E., & Zaldarriaga, M. 2004, *Phys. Rev. D*, 69, 103513

Scoccimarro, R., Sheth, R. K., Hui, L., & Jain, B. 2001, *ApJ*, 546, 20

Semenaitė, A., Sánchez, A. G., Pezzotta, A., et al. 2022, *MNRAS*, 512, 5657

Senatore, L. & Zaldarriaga, M. 2014, *arXiv:1409.1225*

Senatore, L. & Zaldarriaga, M. 2015, *JCAP*, 02, 013

Skilling, J. 2006, *Bayesian Analysis*, 1, 833

Smith, A., de Mattia, A., Burtin, E., Chuang, C.-H., & Zhao, C. 2021, *MNRAS*, 500, 259

Smith, R. E., Scoccimarro, R., & Sheth, R. K. 2007, *Phys. Rev. D*, 75, 063512

Szalay, A. S. 1988, *ApJ*, 333, 21

Taruya, A., Nishimichi, T., & Saito, S. 2010, *Phys. Rev. D*, 82, 063522

Taruya, A. & Soda, J. 1999, *ApJ*, 522, 46

Wadekar, D., Ivanov, M. M., & Scoccimarro, R. 2020, *Phys. Rev. D*, 102, 123521

Wang, Y. 2008, *Phys. Rev. D*, 77, 123525

York, D. G., Adelman, J., Anderson, John E., et al. 2000, *AJ*, 120, 1579

Zel'dovich, Y. B. 1970, *A&A*, 5, 84

Zennaro, M., Angulo, R. E., Contreras, S., Pellejero-Ibañez, M., & Maion, F. 2022, *MNRAS*, 514, 5443

Zennaro, M., Angulo, R. E., Pellejero-Ibañez, M., et al. 2023, *MNRAS*, 524, 2407

¹ IFPU, Institute for Fundamental Physics of the Universe, via Beirut 2, 34151 Trieste, Italy

² SISSA, International School for Advanced Studies, Via Bonomea 265, 34136 Trieste TS, Italy

³ Institute of Space Sciences (ICE, CSIC), Campus UAB, Carrer de Can Magrans, s/n, 08193 Barcelona, Spain

⁴ Institut d'Estudis Espacials de Catalunya (IEEC), Edifici RDIT, Campus UPC, 08860 Castelldefels, Barcelona, Spain

⁵ INAF-Osservatorio Astronomico di Trieste, Via G. B. Tiepolo 11, 34143 Trieste, Italy

⁶ Institute for Astronomy, University of Edinburgh, Royal Observatory, Blackford Hill, Edinburgh EH9 3HJ, UK

⁷ Donostia International Physics Center (DIPC), Paseo Manuel de Lardizabal, 4, 20018, Donostia-San Sebastián, Guipuzkoa, Spain

⁸ IKERBASQUE, Basque Foundation for Science, 48013, Bilbao, Spain

⁹ INAF-Osservatorio Astronomico di Brera, Via Brera 28, 20122 Milano, Italy

¹⁰ Universität Bonn, Argelander-Institut für Astronomie, Auf dem Hügel 71, 53121 Bonn, Germany

¹¹ INFN, Sezione di Trieste, Via Valerio 2, 34127 Trieste TS, Italy

¹² Laboratoire d'Annecy-le-Vieux de Physique Théorique, CNRS & Université Savoie Mont Blanc, 9 Chemin de Bellevue, BP 110, Annecy-le-Vieux, 74941 ANNECY Cedex, France

¹³ Department of Physics, Oxford University, Keble Road, Oxford OX1 3RH, UK

¹⁴ Université Paris-Saclay, Université Paris Cité, CEA, CNRS, AIM, 91191, Gif-sur-Yvette, France

¹⁵ Université de Genève, Département de Physique Théorique and Centre for Astroparticle Physics, 24 quai Ernest-Ansermet, CH-1211 Genève 4, Switzerland

¹⁶ Dipartimento di Scienze Matematiche, Fisiche e Informatiche, Università di Parma, Viale delle Scienze 7/A 43124 Parma, Italy

¹⁷ INFN Gruppo Collegato di Parma, Viale delle Scienze 7/A 43124 Parma, Italy

¹⁸ Technion Israel Institute of Technology, Israel

¹⁹ Aix-Marseille Université, CNRS, CNES, LAM, Marseille, France

²⁰ Dipartimento di Fisica e Astronomia, Università di Bologna, Via Gobetti 93/2, 40129 Bologna, Italy

²¹ INAF-Osservatorio di Astrofisica e Scienza dello Spazio di Bologna, Via Piero Gobetti 93/3, 40129 Bologna, Italy

²² Dipartimento di Fisica "Aldo Pontremoli", Università degli Studi di Milano, Via Celoria 16, 20133 Milano, Italy

²³ Dipartimento di Fisica - Sezione di Astronomia, Università di Trieste, Via Tiepolo 11, 34131 Trieste, Italy

²⁴ ICSC - Centro Nazionale di Ricerca in High Performance Computing, Big Data e Quantum Computing, Via Magnanelli 2, Bologna, Italy

²⁵ INFN-Sezione di Genova, Via Dodecaneso 33, 16146, Genova, Italy

²⁶ Dipartimento di Fisica, Università di Genova, Via Dodecaneso 33, 16146, Genova, Italy

²⁷ ESAC/ESA, Camino Bajo del Castillo, s/n., Urb. Villafranca del Castillo, 28692 Villanueva de la Cañada, Madrid, Spain

²⁸ INFN-Sezione di Bologna, Viale Berti Pichat 6/2, 40127 Bologna, Italy

²⁹ Max Planck Institute for Extraterrestrial Physics, Giessenbachstr. 1, 85748 Garching, Germany

³⁰ Universitäts-Sternwarte München, Fakultät für Physik, Ludwig-Maximilians-Universität München, Scheinerstr. 1, 81679 München, Germany

³¹ Department of Physics "E. Pancini", University Federico II, Via Cinthia 6, 80126, Napoli, Italy

³² INAF-Osservatorio Astronomico di Capodimonte, Via Moiariello 16, 80131 Napoli, Italy

³³ Dipartimento di Fisica, Università degli Studi di Torino, Via P. Giuria 1, 10125 Torino, Italy

³⁴ INFN-Sezione di Torino, Via P. Giuria 1, 10125 Torino, Italy

³⁵ INAF-Osservatorio Astrofisico di Torino, Via Osservatorio 20, 10025 Pino Torinese (TO), Italy

³⁶ INAF-IASF Milano, Via Alfonso Corti 12, 20133 Milano, Italy

³⁷ INAF-Osservatorio Astronomico di Roma, Via Frascati 33, 00078 Monteporzio Catone, Italy

³⁸ INFN-Sezione di Roma, Piazzale Aldo Moro, 2 - c/o Dipartimento di Fisica, Edificio G. Marconi, 00185 Roma, Italy

³⁹ Centro de Investigaciones Energéticas, Medioambientales y Tecnológicas (CIEMAT), Avenida Complutense 40, 28040 Madrid, Spain

⁴⁰ Port d'Informació Científica, Campus UAB, C. Albareda s/n, 08193 Bellaterra (Barcelona), Spain

⁴¹ Institute for Theoretical Particle Physics and Cosmology (TTK), RWTH Aachen University, 52056 Aachen, Germany

⁴² Deutsches Zentrum für Luft- und Raumfahrt e. V. (DLR), Linder Höhe, 51147 Köln, Germany

⁴³ INFN section of Naples, Via Cinthia 6, 80126, Napoli, Italy

⁴⁴ Institute for Astronomy, University of Hawaii, 2680 Woodlawn Drive, Honolulu, HI 96822, USA

⁴⁵ Dipartimento di Fisica e Astronomia "Augusto Righi" - Alma Mater Studiorum Università di Bologna, Viale Berti Pichat 6/2, 40127 Bologna, Italy

⁴⁶ Instituto de Astrofísica de Canarias, E-38205 La Laguna, Tenerife, Spain

⁴⁷ European Space Agency/ESRIN, Largo Galileo Galilei 1, 00044 Frascati, Roma, Italy

⁴⁸ Université Claude Bernard Lyon 1, CNRS/IN2P3, IP2I Lyon, UMR 5822, Villeurbanne, F-69100, France

⁴⁹ Institut de Ciències del Cosmos (ICCUB), Universitat de Barcelona (IEEC-UB), Martí i Franquès 1, 08028 Barcelona, Spain

⁵⁰ Institució Catalana de Recerca i Estudis Avançats (ICREA), Passeig de Lluís Companys 23, 08010 Barcelona, Spain

⁵¹ UCB Lyon 1, CNRS/IN2P3, IUF, IP2I Lyon, 4 rue Enrico Fermi, 69622 Villeurbanne, France

⁵² Department of Astronomy, University of Geneva, ch. d'Ecogia 16, 1290 Versoix, Switzerland

⁵³ Université Paris-Saclay, CNRS, Institut d'astrophysique spatiale, 91405, Orsay, France

⁵⁴ INFN-Padova, Via Marzolo 8, 35131 Padova, Italy

⁵⁵ Aix-Marseille Université, CNRS/IN2P3, CPPM, Marseille, France

⁵⁶ INAF-Istituto di Astrofisica e Planetologia Spaziali, via del Fosso del Cavaliere, 100, 00100 Roma, Italy

⁵⁷ INFN-Bologna, Via Irnerio 46, 40126 Bologna, Italy

⁵⁸ School of Physics, HH Wills Physics Laboratory, University of Bristol, Tyndall Avenue, Bristol, BS8 1TL, UK

⁵⁹ University Observatory, LMU Faculty of Physics, Scheinerstr. 1, 81679 Munich, Germany

⁶⁰ INAF-Osservatorio Astronomico di Padova, Via dell'Osservatorio 5, 35122 Padova, Italy

⁶¹ INFN-Sezione di Milano, Via Celoria 16, 20133 Milano, Italy

⁶² Institute of Theoretical Astrophysics, University of Oslo, P.O. Box 1029 Blindern, 0315 Oslo, Norway

⁶³ Jet Propulsion Laboratory, California Institute of Technology, 4800 Oak Grove Drive, Pasadena, CA, 91109, USA

⁶⁴ Felix Hormuth Engineering, Goethestr. 17, 69181 Leimen, Germany

⁶⁵ Technical University of Denmark, Elektrovej 327, 2800 Kgs. Lyngby, Denmark

⁶⁶ Cosmic Dawn Center (DAWN), Denmark

⁶⁷ Max-Planck-Institut für Astronomie, Königstuhl 17, 69117 Heidelberg, Germany

⁶⁸ Department of Physics and Astronomy, University College London, Gower Street, London WC1E 6BT, UK

⁶⁹ Department of Physics, P.O. Box 64, University of Helsinki, 00014 Helsinki, Finland

⁷⁰ Helsinki Institute of Physics, Gustaf Hällströminkatu 2, University of Helsinki, 00014 Helsinki, Finland

⁷¹ Laboratoire d'étude de l'Univers et des phénomènes eXtremes, Observatoire de Paris, Université PSL, Sorbonne Université, CNRS, 92190 Meudon, France

⁷² SKAO, Jodrell Bank, Lower Withington, Macclesfield SK11 9FT, UK

⁷³ Centre de Calcul de l'IN2P3/CNRS, 21 avenue Pierre de Coubertin 69627 Villeurbanne Cedex, France

⁷⁴ University of Applied Sciences and Arts of Northwestern Switzerland, School of Computer Science, 5210 Windisch, Switzerland

⁷⁵ Dipartimento di Fisica e Astronomia "Augusto Righi" - Alma Mater Studiorum Università di Bologna, via Piero Gobetti 93/2, 40129 Bologna, Italy

⁷⁶ Department of Physics, Institute for Computational Cosmology, Durham University, South Road, Durham, DH1 3LE, UK

⁷⁷ University of Applied Sciences and Arts of Northwestern Switzerland, School of Engineering, 5210 Windisch, Switzerland

⁷⁸ Institute of Physics, Laboratory of Astrophysics, Ecole Polytechnique Fédérale de Lausanne (EPFL), Observatoire de Sauverny, 1290 Versoix, Switzerland

⁷⁹ Telespazio UK S.L. for European Space Agency (ESA), Camino bajo del Castillo, s/n, Urbanizacion Villafranca del Castillo, Villanueva de la Cañada, 28692 Madrid, Spain

⁸⁰ Institut de Física d'Altes Energies (IFAE), The Barcelona Institute of Science and Technology, Campus UAB, 08193 Bellaterra (Barcelona), Spain

⁸¹ European Space Agency/ESTEC, Keplerlaan 1, 2201 AZ Noordwijk, The Netherlands

⁸² DARK, Niels Bohr Institute, University of Copenhagen, Jagtvej 155, 2200 Copenhagen, Denmark

⁸³ Waterloo Centre for Astrophysics, University of Waterloo, Waterloo, Ontario N2L 3G1, Canada

⁸⁴ Department of Physics and Astronomy, University of Waterloo, Waterloo, Ontario N2L 3G1, Canada

⁸⁵ Perimeter Institute for Theoretical Physics, Waterloo, Ontario N2L 2Y5, Canada

⁸⁶ Space Science Data Center, Italian Space Agency, via del Politecnico snc, 00133 Roma, Italy

87 Centre National d'Etudes Spatiales – Centre spatial de Toulouse,
18 avenue Edouard Belin, 31401 Toulouse Cedex 9, France

88 Institute of Space Science, Str. Atomistilor, nr. 409 Măgurele, Ilfov,
077125, Romania

89 Instituto de Física Teórica UAM-CSIC, Campus de Cantoblanco,
28049 Madrid, Spain

90 Institut de Recherche en Astrophysique et Planétologie (IRAP),
Université de Toulouse, CNRS, UPS, CNES, 14 Av. Edouard Belin,
31400 Toulouse, France

91 Université St Joseph; Faculty of Sciences, Beirut, Lebanon

92 Departamento de Física, FCFM, Universidad de Chile, Blanco Encalada 2008, Santiago, Chile

93 Department of Physics and Helsinki Institute of Physics, Gustaf
Hällströmin katu 2, University of Helsinki, 00014 Helsinki, Finland

94 Dipartimento di Fisica e Astronomia "G. Galilei", Università di
Padova, Via Marzolo 8, 35131 Padova, Italy

95 Department of Physics, Royal Holloway, University of London,
Surrey TW20 0EX, UK

96 Departamento de Física, Faculdade de Ciências, Universidade de
Lisboa, Edifício C8, Campo Grande, PT1749-016 Lisboa, Portugal

97 Instituto de Astrofísica e Ciências do Espaço, Faculdade de Ciências,
Universidade de Lisboa, Tapada da Ajuda, 1349-018 Lisboa,
Portugal

98 Mullard Space Science Laboratory, University College London,
Holmbury St Mary, Dorking, Surrey RH5 6NT, UK

99 Cosmic Dawn Center (DAWN)

100 Niels Bohr Institute, University of Copenhagen, Jagtvej 128, 2200
Copenhagen, Denmark

101 Universidad Politécnica de Cartagena, Departamento de Elec-
trónica y Tecnología de Computadoras, Plaza del Hospital 1, 30202
Cartagena, Spain

102 Caltech/IPAC, 1200 E. California Blvd., Pasadena, CA 91125,
USA

103 Dipartimento di Fisica e Scienze della Terra, Università degli Studi
di Ferrara, Via Giuseppe Saragat 1, 44122 Ferrara, Italy

104 Istituto Nazionale di Fisica Nucleare, Sezione di Ferrara, Via
Giuseppe Saragat 1, 44122 Ferrara, Italy

105 Université Paris Cité, CNRS, Astroparticule et Cosmologie, 75013
Paris, France

106 INAF, Istituto di Radioastronomia, Via Piero Gobetti 101, 40129
Bologna, Italy

107 Astronomical Observatory of the Autonomous Region of the Aosta
Valley (OAVdA), Loc. Lignan 39, I-11020, Nus (Aosta Valley),
Italy

108 Université Côte d'Azur, Observatoire de la Côte d'Azur, CNRS,
Laboratoire Lagrange, Bd de l'Observatoire, CS 34229, 06304
Nice cedex 4, France

109 Univ. Grenoble Alpes, CNRS, Grenoble INP, LPSC-IN2P3, 53, Av-
enue des Martyrs, 38000, Grenoble, France

110 Dipartimento di Fisica, Sapienza Università di Roma, Piazzale
Aldo Moro 2, 00185 Roma, Italy

111 Aurora Technology for European Space Agency (ESA), Camino
bajo del Castillo, s/n, Urbanizacion Villafranca del Castillo, Vil-
lanueva de la Cañada, 28692 Madrid, Spain

112 Department of Mathematics and Physics E. De Giorgi, University
of Salento, Via per Arnesano, CP-I93, 73100, Lecce, Italy

113 INFN, Sezione di Lecce, Via per Arnesano, CP-193, 73100, Lecce,
Italy

114 INAF-Sezione di Lecce, c/o Dipartimento Matematica e Fisica, Via
per Arnesano, 73100, Lecce, Italy

115 Institut d'Astrophysique de Paris, 98bis Boulevard Arago, 75014,
Paris, France

116 ICL, Junia, Université Catholique de Lille, LITL, 59000 Lille,
France

117 CERCA/ISO, Department of Physics, Case Western Reserve Uni-
versity, 10900 Euclid Avenue, Cleveland, OH 44106, USA

118 Departamento de Física Fundamental. Universidad de Salamanca.
Plaza de la Merced s/n. 37008 Salamanca, Spain

119 Aix-Marseille Université, Université de Toulon, CNRS, CPT, Mar-
seille, France

120 Université de Strasbourg, CNRS, Observatoire astronomique de
Strasbourg, UMR 7550, 67000 Strasbourg, France

121 Center for Data-Driven Discovery, Kavli ITPU (WPI), UTIAS,
The University of Tokyo, Kashiwa, Chiba 277-8583, Japan

122 Max-Planck-Institut für Physik, Boltzmannstr. 8, 85748 Garching,
Germany

123 Jodrell Bank Centre for Astrophysics, Department of Physics and
Astronomy, University of Manchester, Oxford Road, Manchester
M13 9PL, UK

124 California Institute of Technology, 1200 E California Blvd,
Pasadena, CA 91125, USA

125 Department of Physics & Astronomy, University of California
Irvine, Irvine CA 92697, USA

126 Kapteyn Astronomical Institute, University of Groningen, PO Box
800, 9700 AV Groningen, The Netherlands

127 Departamento Física Aplicada, Universidad Politécnica de Carta-
gena, Campus Muralla del Mar, 30202 Cartagena, Murcia, Spain

128 Instituto de Física de Cantabria, Edificio Juan Jordá, Avenida de los
Castros, 39005 Santander, Spain

129 Institute of Cosmology and Gravitation, University of Portsmouth,
Portsmouth PO1 3FX, UK

130 Department of Computer Science, Aalto University, PO Box
15400, Espoo, FI-00 076, Finland

131 Universidad de La Laguna, Dpto. Astrofísica, E-38206 La Laguna,
Tenerife, Spain

132 Ruhr University Bochum, Faculty of Physics and Astronomy, As-
tronomical Institute (AIRUB), German Centre for Cosmological
Lensing (GCCL), 44780 Bochum, Germany

133 Department of Physics and Astronomy, Vesilinnantie 5, University
of Turku, 20014 Turku, Finland

134 Serco for European Space Agency (ESA), Camino bajo del
Castillo, s/n, Urbanizacion Villafranca del Castillo, Villanueva de
la Cañada, 28692 Madrid, Spain

135 ARC Centre of Excellence for Dark Matter Particle Physics, Mel-
bourne, Australia

136 Centre for Astrophysics & Supercomputing, Swinburne University
of Technology, Hawthorn, Victoria 3122, Australia

137 Department of Physics and Astronomy, University of the Western
Cape, Bellville, Cape Town, 7535, South Africa

138 DAMTP, Centre for Mathematical Sciences, Wilberforce Road,
Cambridge CB3 0WA, UK

139 Kavli Institute for Cosmology Cambridge, Madingley Road, Cam-
bridge, CB3 0HA, UK

140 Institut d'Astrophysique de Paris, UMR 7095, CNRS, and Sor-
bonne Université, 98 bis boulevard Arago, 75014 Paris, France

141 Departement of Theoretical Physics, University of Geneva,
Switzerland

142 Department of Physics, Centre for Extragalactic Astronomy,
Durham University, South Road, Durham, DH1 3LE, UK

143 IRFU, CEA, Université Paris-Saclay 91191 Gif-sur-Yvette Cedex,
France

144 INAF-Osservatorio Astrofisico di Arcetri, Largo E. Fermi 5, 50125,
Firenze, Italy

145 Centro de Astrofísica da Universidade do Porto, Rua das Estrelas,
4150-762 Porto, Portugal

146 Instituto de Astrofísica e Ciências do Espaço, Universidade do
Porto, CAUP, Rua das Estrelas, PT4150-762 Porto, Portugal

147 HE Space for European Space Agency (ESA), Camino bajo del
Castillo, s/n, Urbanizacion Villafranca del Castillo, Villanueva de
la Cañada, 28692 Madrid, Spain

148 Department of Astrophysics, University of Zurich, Winterthurer-
strasse 190, 8057 Zurich, Switzerland

149 INAF - Osservatorio Astronomico d'Abruzzo, Via Maggini, 64100,
Teramo, Italy

150 Theoretical astrophysics, Department of Physics and Astronomy,
Uppsala University, Box 516, 751 37 Uppsala, Sweden

151 Mathematical Institute, University of Leiden, Einsteinweg 55, 2333
CA Leiden, The Netherlands

152 Leiden Observatory, Leiden University, Einsteinweg 55, 2333 CC
Leiden, The Netherlands

¹⁵³ Institute of Astronomy, University of Cambridge, Madingley Road, Cambridge CB3 0HA, UK
¹⁵⁴ Center for Astrophysics and Cosmology, University of Nova Gorica, Nova Gorica, Slovenia
¹⁵⁵ Institute for Particle Physics and Astrophysics, Dept. of Physics, ETH Zurich, Wolfgang-Pauli-Strasse 27, 8093 Zurich, Switzerland
¹⁵⁶ Department of Astrophysical Sciences, Peyton Hall, Princeton University, Princeton, NJ 08544, USA
¹⁵⁷ Institut de Physique Théorique, CEA, CNRS, Université Paris-Saclay 91191 Gif-sur-Yvette Cedex, France
¹⁵⁸ International Centre for Theoretical Physics (ICTP), Strada Costiera 11, 34151 Trieste, Italy
¹⁵⁹ Center for Computational Astrophysics, Flatiron Institute, 162 5th Avenue, 10010, New York, NY, USA

Appendix A: Hybrid model performance at higher precision level

The BACCO emulator employs neural networks to interpolate predictions from a hybrid bias model across a range of cosmological parameters, using outputs from cosmologically rescaled N -body simulations (Angulo & White 2010). To ensure accuracy across cosmologies, we normalise the simulation outputs using a basis of PT predictions, which reduces the dynamical range of the multipoles of the 15 bias terms.

To build the full hybrid model prediction, we multiply the simulation-based emulator outputs by their corresponding PT predictions evaluated at the target cosmology. Two theoretical models are used to compute the baseline spectra: a linear smeared BAO model for matter-only statistics (Angulo et al. 2021), and the Lagrangian Perturbation Theory (LPT) predictions implemented in *Velocileptors* (Chen et al. 2020). However, computing the analytical predictions is a computational bottleneck. To address this, we constructed separate emulators for each theoretical component.

Initially in BACCO, the PT emulators were constructed using a coarser k -binning, consisting of 50 logarithmically spaced bins over the range $k \in [0.001, 1] h \text{ Mpc}^{-1}$. In contrast, the N -body emulators used a finer binning of 100 logarithmically spaced bins over the same k -range. To reconcile this mismatch when building the hybrid prediction, we interpolated between the two sets of components. This approach proved sufficient for earlier applications involving survey data, where the power spectrum is typically measured on a linear binning with $\Delta k = 0.005 h \text{ Mpc}^{-1}$. However, the Flagship simulation employs a much finer k -binning, with $\Delta k = 0.0016 h \text{ Mpc}^{-1}$. This denser sampling requires the PT emulators to be interpolated at most k -points, leading to small but systematic biases in the model predictions when using a coarser k -binning.

To mitigate these biases, we implemented two key improvements: (1) we regenerated the perturbation theory emulators using the same k -binning as the N -body emulator, and (2) we adopted a modified neural-network architecture better suited for this task. In particular, we replaced the PCA-based input with the full power spectra, leveraging the smoothness of the perturbation theory predictions. Additionally, we increased the size of the hidden layer from 35 to 150 neurons to enhance the capacity of the model. These modifications led to a significant improvement in accuracy, as demonstrated in Fig. A.1. In this figure, we illustrate the differences between the old and new interpolation strategies, shown relative to the expected monopole uncertainties for the Flagship and *Euclid* volumes. In the left panels, the old strategy exhibits artificial oscillations – visible as wiggles – as well as scale-dependent tensions between large and small scales, particularly at the lowest and highest redshifts. Regardless of interpolation version, additional artifacts appear in the hexadecapole at redshifts $z \gtrsim 1.5$. Although these effects are smaller than the expected hexadecapole uncertainties, we adopt a conservative approach and limit our analysis to the monopole and quadrupole only.

While the updated interpolation method significantly reduces these issues, residual deviations of the same order as the Flagship volume uncertainties persist on scales around $k_{\text{max}} = 0.4 h \text{ Mpc}^{-1}$. For this reason, we restricted our BACCO analysis to the *Euclid* volume. Achieving the precision required for a full Flagship-volume analysis will require further developments in our emulator methodology, which we leave for future work.

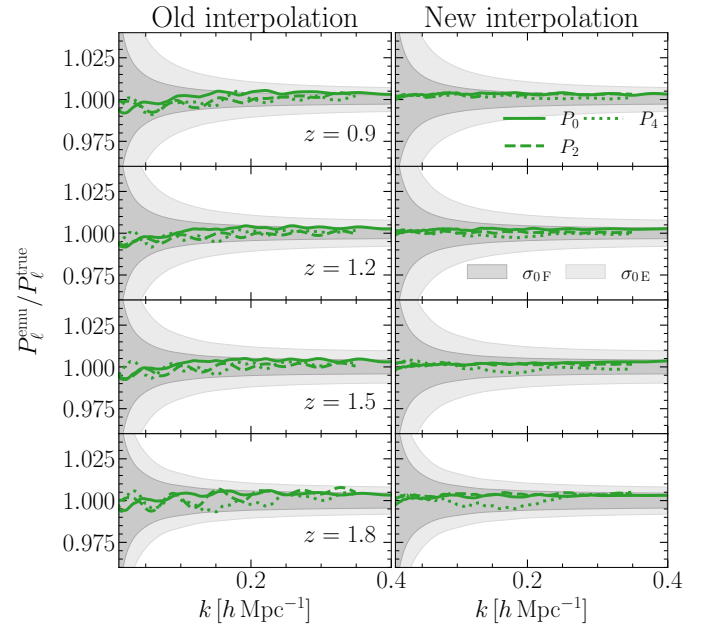


Fig. A.1. Accuracy of the previous and updated implementations of the PT emulators in BACCO, compared to the direct (‘true’) evaluation of the PT model. Grey shaded regions indicate the expected uncertainties for the monopole of the Flagship (F) and *Euclid* (E) survey volumes. Rows correspond to different redshifts, while columns compare the old and new interpolation strategies. Oscillatory artifacts and scale-dependent tilts present in the older approach are significantly reduced with the updated method. Some artifacts are still present in the hexadecapole at intermediate scales and higher redshifts.

Appendix B: 2-dimensional posteriors exploration

A more detailed examination of the influence of prior relations on non-local biases is presented in Fig. B.1, which directly shows the 2-dimensional marginalised posteriors for a subset of parameters. The top and bottom panels correspond to the EFT and VDG $_{\infty}$ models, respectively. Different colours indicate the maximum wave mode k_{max} of the fit, while each row refers to a different treatment of the tidal bias parameters. In addition to the cosmological parameters, we also show the posterior distribution of b_1 and N_0^P , since these parameters are significantly degenerate with A_s . Additionally, we include b_2 to have a more comprehensive picture for the local bias parameters. The fiducial values of the cosmological parameters are shown with dashed lines, along with the large-scale limit values for b_1 and N_0^P recovered from real-space fits of the matter power spectrum (see *Euclid Collaboration: Pezzotta et al. 2024*, for a detailed explanation on this derivation). For compactness, we only display the results for the $z = 1.5$ snapshot, since it corresponds to the median redshift of *Euclid*.

In the EFT analysis (top panel), with all biases allowed to vary freely, we find that A_s is biased at the 2σ level. On the other hand, h and ω_c are biased at most at the 1σ level. As expected, the linear bias shows a strong degeneracy with A_s and exhibits significant bias when fitting smaller scales. Interestingly, the constant shot-noise parameter is generally recovered at the 1σ level, and b_2 remains stable. When fixing γ_{21} , ω_c is slightly better constrained at larger scales, but at the cost of introducing bi-modalities in b_2 at intermediate scales and recovering negative values at smaller scales. Notice that such behaviour appears on scales where the FoB already starts to increase, indicating a breakdown of the model. Since the directions of these bi-

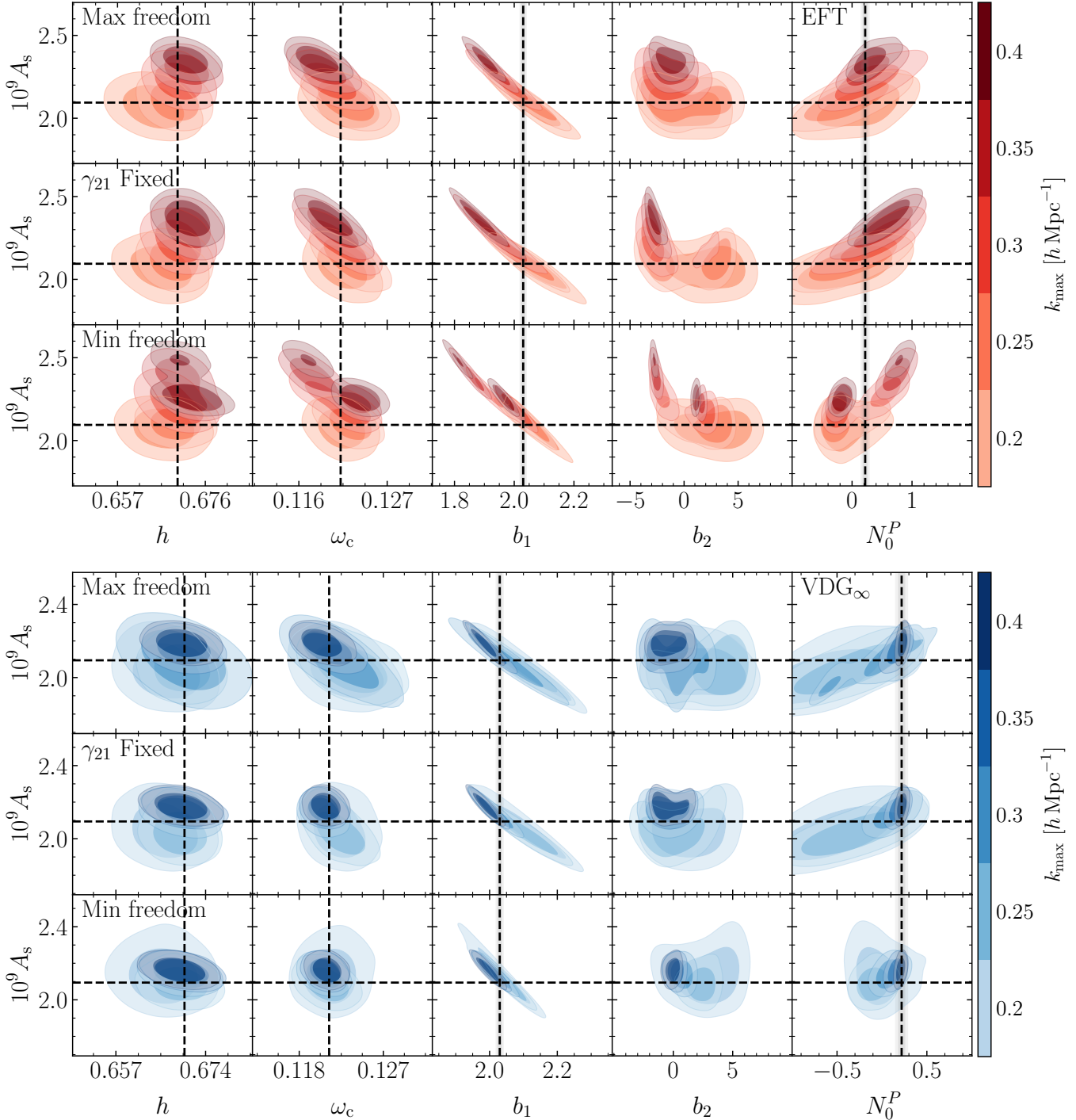


Fig. B.1. 2-dimensional marginalised posterior distributions for the $z = 1.5$ snapshot. Cosmological parameters (h , ω_c , A_s) are shown, along with the linear and second-order local biases and the scale-independent shot-noise parameter. The *top and bottom panels* correspond to the EFT and VDG_∞ models, respectively. Different colours indicate the maximum wave mode of the fit, as indicated by the colour bar. From top to bottom, *different rows* show the impact of imposing relations on the tidal biases γ_2 and γ_{21} . Fiducial values of the cosmological parameters are indicated with dashed vertical and horizontal lines. For b_1 and N_0^P , dashed lines indicate the best-fit parameters obtained from the large-scale limit of the matter power spectrum (see text for details).

modalities are orthogonal to A_s , it is unlikely that they introduce additional biases in this parameter. Furthermore, the constraint on the constant noise parameter is also degraded in this regime. Finally, fixing both tidal biases introduces bi-modalities across all displayed parameters at smaller scales, with N_0^P also deviating from its fiducial value. As a final note, we recall that the bi-modalities in the cosmological parameters appear on scales

where the model is already breaking down in terms of FoB, as shown in Fig. 2. Moreover, fixing only γ_2 to the excursion-set relation increases the constraining power on N_0^P and b_2 , but the impact on cosmological parameters is negligible. As a consequence – and because previous works analysing the power spectrum plus bispectrum (e.g. Eggemeier et al. 2021) have shown that this is

not, in general, a good approximation – we do not include this case in the plot.

For the VDG_∞ case (bottom panels of Fig. B.1), the main conclusion is that the posteriors exhibit an improved behaviour across all bias configurations, as there is no significant parameter drift from their fiducial values nor strong bi-modalities. The most notable feature is that fixing γ_{21} reduces the degeneracies in the A_s - ω_c plane and significantly tightens the constraints on the N_0^P parameter compared to the maximal-freedom scenario (at the same k_{\max}). Furthermore, fixing both tidal biases simultaneously results in less biased and tighter posterior distributions, thereby lowering the FoB and substantially increasing the FoM in the minimal-freedom scenario. However, when compared to the intermediate configuration that only fixes γ_{21} , the additional gain appears marginal, as already observed in Fig. 2. For completeness, although this case is not displayed, we have tested that fixing γ_2 does not by itself have any significant impact on the cosmological parameters, in the sense that the marginalised 2-dimensional posteriors do not change appreciably compared to the maximal-freedom case.

For the purpose of model validation and comparison, our focus is on recovering cosmological parameters without introducing additional biases arising from the breakdown of the adopted bias relations. As shown in Fig. B.1, the fiducial cosmological parameters are better recovered for both PT models when γ_{21} is fixed, compared to the minimal-freedom scenario, which introduces additional bi-modalities in the EFT case. Thus, we adopt fixing γ_{21} as a robust baseline choice for the comparisons presented in Sect. 6.

Finally, we recall that similar conclusions hold for the four different redshifts explored in this work, for completeness we present violin plots with the 1D marginalised posterior distributions in Appendix C.

Appendix C: 1-dimensional posteriors exploration

In the first three rows of Fig. C.1, we show the violin plots for the three cosmological parameters corresponding to the minimal bias case. In the same figure, the fourth row shows the significance at which each parameter is recovered. This plot allows us to visualise, in a more compact way, the 1-dimensional marginalised posterior distributions for each parameter, each value of k_{\max} , each RSD model, and each redshift.

In the first panel, focusing on the red symbols, which correspond to the EFT case, we see that in terms of bias and constraining power, h is the most stably recovered parameter across all scales and redshifts. Moreover, in the bottom panel we see that it is the parameter whose constraining power saturates earliest. Looking at the second and third rows, we observe that the bi-modalities seen for EFT in Fig. B.1 for the snapshot at $z = 1.5$ also appear, to some degree, in all snapshots except the lowest redshift one, where only mild skewness remains. These bi-modalities are also responsible for reducing the gain in constraining power for both parameters, as illustrated in the bottom panel. Another interesting feature of this plot is that it allows us to assess the impact of projection effects (see Appendix F for more details), since both the mean marginalised parameter and the maximum-a-posteriori estimate – where the likelihood is maximised – are shown. Notice that in most cases both the mean marginalised value and the maximum-a-posteriori value lie within the 68% confidence interval.

Turning now to the blue symbols, which correspond to the VDG_∞ case, we see that the posterior distributions are generally

better behaved: they look more Gaussian, lie closer to the fiducial values, and tighten when adding information from smaller scales without biasing the parameters. One additional feature to note is that, at the highest redshift, the maximum-a-posteriori estimate lies slightly outside the 68% interval relative to the mean marginalised value; however, this effect disappears once the model includes information from sufficiently small scales, leading to improved posterior distributions. Finally, the gain in constraining power is more stable for this model, and we recover most of the available information for each parameter by $k_{\max} = 0.4 h \text{ Mpc}^{-1}$, since the errors tend to flatten at smaller scales – with the only exception of A_s at the highest redshift.

Appendix D: Hexadecapole information

In our baseline comparison of the RSD models presented in Sect. 6.1, we used information from the first three even multipoles (P_0 , P_2 , and P_4). Here, we validate that this configuration is optimal for our study.

In Fig. D.1, we show that for the maximal bias case, neglecting the information from the hexadecapole leads to only marginal changes in the FoB and FoM. Nonetheless, the p -value is consistently degraded, indicating a poorer description of the dataset. This degradation in the goodness-of-fit arises because the hexadecapole helps to better constrain the nuisance parameters. Even though the cosmological constraints remain essentially unchanged, tighter constraints on the full parameter space allow the model to provide a more accurate description of the dataset as a whole.

Appendix E: Comparison between BACCO and VDG_∞ priors

The results discussed in Sect. 6.1, primarily those shown in Fig. 6, appear unexpected: the conclusions do not fully agree with our baseline analysis, and the information extracted by BACCO saturates at larger-than-expected scales. Here we describe several potential sources of spurious constraints in the analysis.

One of the main differences in the perturbation-theory scheme between BACCO and VDG_∞ is the large-scale normalisation imposed on the $\delta^2 \delta^2$ term, as described in Eq. (34) of Pezzotta et al. (2021). This correction is not applied in BACCO; instead, BACCO subtracts the mean of the δ^2 field to build the $\delta^2 \delta^2$ contribution (see Eq. 1 in Pellejero Ibañez et al. 2024). We explicitly removed this normalisation in VDG_∞ and repeated one of the analyses at large scales; we found that this difference is not the primary cause of the extra constraining power seen in BACCO at large scales. Nonetheless, and although the effect is minor, the normalisation in VDG_∞ does impact mainly the recovered bias parameters.

Another significant difference between VDG_∞ and BACCO is the absence of counterterms in the BACCO approach. We repeated one of the VDG_∞ analyses while omitting the counterterms and found that the gain in constraining power on cosmological parameters was not significant. Therefore, we conclude that counterterms are unlikely to be responsible for the tighter cosmological constraints seen in BACCO.

An additional difference concerns the priors adopted in the BACCO runs, which were tighter for some nuisance and cosmological parameters. The cosmology priors were chosen to remain within the emulation range of BACCO; as discussed in Euclid Collaboration: Pezzotta et al. (2024), increasing the emulation range in BACCO is computationally expensive. In particular, the prior on

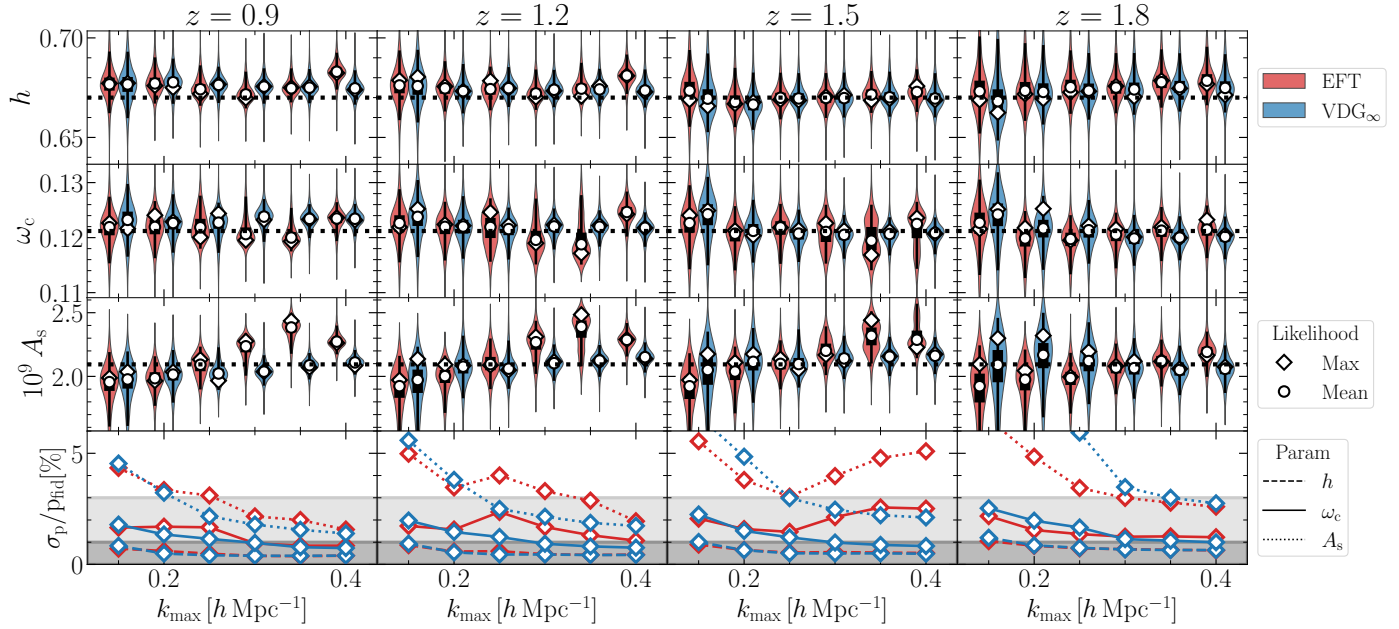


Fig. C.1. Violin plot for the minimal-model fits as a function of the maximum wave mode, k_{\max} . In the first three rows, the circles show the mean marginalised posterior of each parameter (the first row corresponds to h , the second to ω_c , and the third to A_s), while the diamonds correspond to the maximum-a-posteriori point where the full likelihood is maximised. The black boxes and whiskers indicate the 68% and 95% limits, respectively. The blue and red regions show the 1D marginalised distributions for each parameter, for either the EFT or VDG_∞ models, as described in the legend. The bottom panel presents the ratio of the error on each parameter (as indicated on the labels) to its fiducial value. Each column corresponds to a different redshift. The range displayed for each parameter is $h \pm 5\%$, $\omega_c \pm 10\%$, and $A_s \pm 30\%$. For reference, the shaded regions in the bottom panel show the 1% and 3% limits.

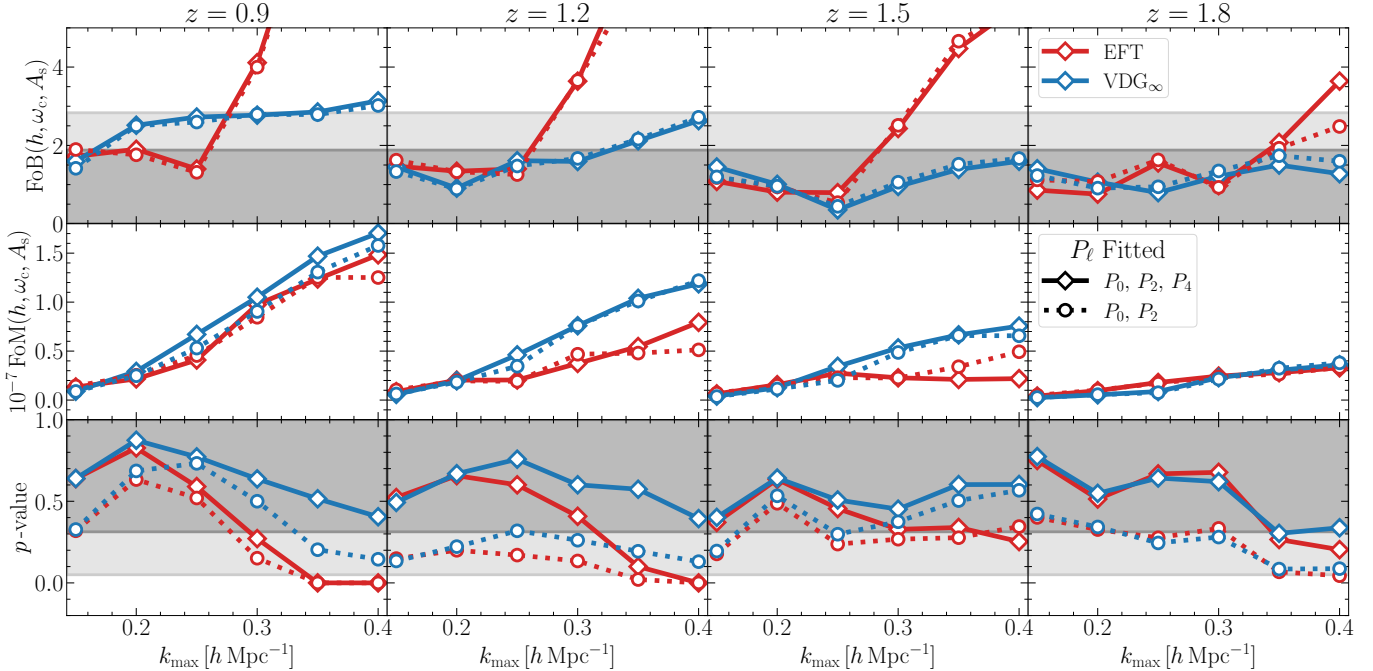


Fig. D.1. Same as Fig. 2, but comparing the impact of neglecting the information from P_4 , indicated by circles and dotted lines.

the scale-dependent noise was noticeably tighter in BACCO. We repeated the VDG_∞ analysis using the BACCO priors and found that, in this case, the priors do affect the results – especially at larger scales and for the nearest redshifts – by producing artificially tighter constraints. Nevertheless, for the remaining redshifts and scales the choice of priors did not significantly alter the conclusions.

Appendix F: Priors impact in the EFT model

As previously mentioned, several recent works (Holm et al. 2023; Carrilho et al. 2023) have shown that in the EFT modelling context, the marginalised posterior distributions of parameters can be strongly affected by prior volume effects. However, Holm et al. (2023) also demonstrated that when analysing a sufficiently large survey volume, these effects become negligible.

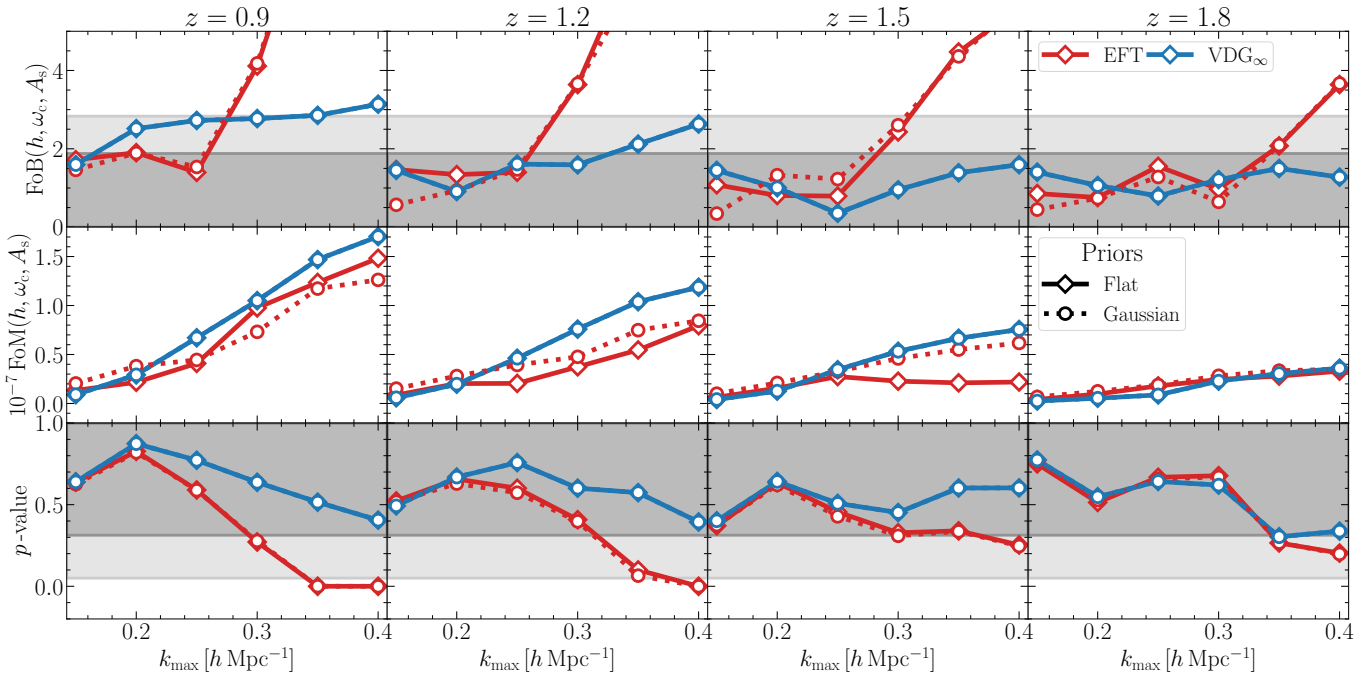


Fig. F.1. Same as Fig. 2, but comparing the impact of imposing Gaussian priors, indicated by circles and dotted lines.

To verify that our analysis is not impacted by such artefacts, we tested the effect of adopting Gaussian priors on all nuisance parameters – as proposed in Philcox & Ivanov (2022) – and compared the results with those obtained using the broad flat priors adopted in our baseline analysis. This test was performed for the EFT model in the minimal-freedom configuration.

Figure F.1 shows that the impact at the level of summary statistics is small. Nevertheless, it is worth noting that imposing Gaussian priors on the nuisance parameters removes the bi-modalities present in N_0^P , b_2 , and the counterterms. However, the disappearance of these bi-modalities does not translate into an improved recovery of the cosmological parameters.

In this work we have carried out only a simple assessment of the impact of prior assumptions, with the goal of confirming that our main conclusions remain robust when wide flat priors are applied. A more systematic study of prior effects is left for future work, particularly in the context of *Euclid* survey specifications. In that configuration, the analysis may be more susceptible to prior volume effects – especially when opening the parameter space to also include models of dynamical dark energy – making it essential to understand their implications and how to mitigate them in order to avoid a prior-dominated inference.

Appendix G: Full posteriors

Here we explicitly show the posterior distributions of the shared parameter space for the three RSD models introduced in Sect. 3.

A key aspect of the cross-validation between the different perturbative models is the level of consistency observed within their common parameter space. Below we summarise the main findings of this comparison, while Fig. G.1 provides an illustrative example of the full posterior distributions.

At intermediate scales ($k_{\max} = 0.20 h \text{ Mpc}^{-1}$), the three models display very similar behaviour for the cosmological parameters. In contrast, EFT and VDG_∞ yield significantly weaker constraints on the bias and noise parameters. This is likely related to BACCO hitting the prior boundaries for b_2 and γ_2 , although this

effect does not appear to significantly impact the cosmological parameters.

When nonlinear scales are included ($k_{\max} = 0.40 h \text{ Mpc}^{-1}$), both the BACCO and VDG_∞ models remain stable and successfully recover the fiducial cosmological parameters. Notably, their posterior distributions for the bias and noise parameters also converge to the same region of parameter space, reinforcing the consistency between these two models at smaller scales. In contrast, the EFT model constrains the higher-order bias parameters in a region that differs from the one preferred by VDG_∞ and BACCO, consistent with the shifts observed in the cosmological posteriors in the main text (see Figs. 5 and 6). Although the constant-noise parameter inferred by EFT is relatively close to the values recovered by VDG_∞ and BACCO, the EFT constraints remain weaker overall.

We notice that the posteriors of VDG_∞ and EFT behave similarly at larger scales in the whole parameter space, but VDG_∞ converges to the posteriors of BACCO at smaller scales; this suggests that the strength of the VDG_∞ model becomes particularly evident in the small-scale regime, where the improved modelling of RSD offers significant advantages. Finally, the level of agreement between VDG_∞ and BACCO at these scales works as a cross-validation of both models in the mildly nonlinear regime.

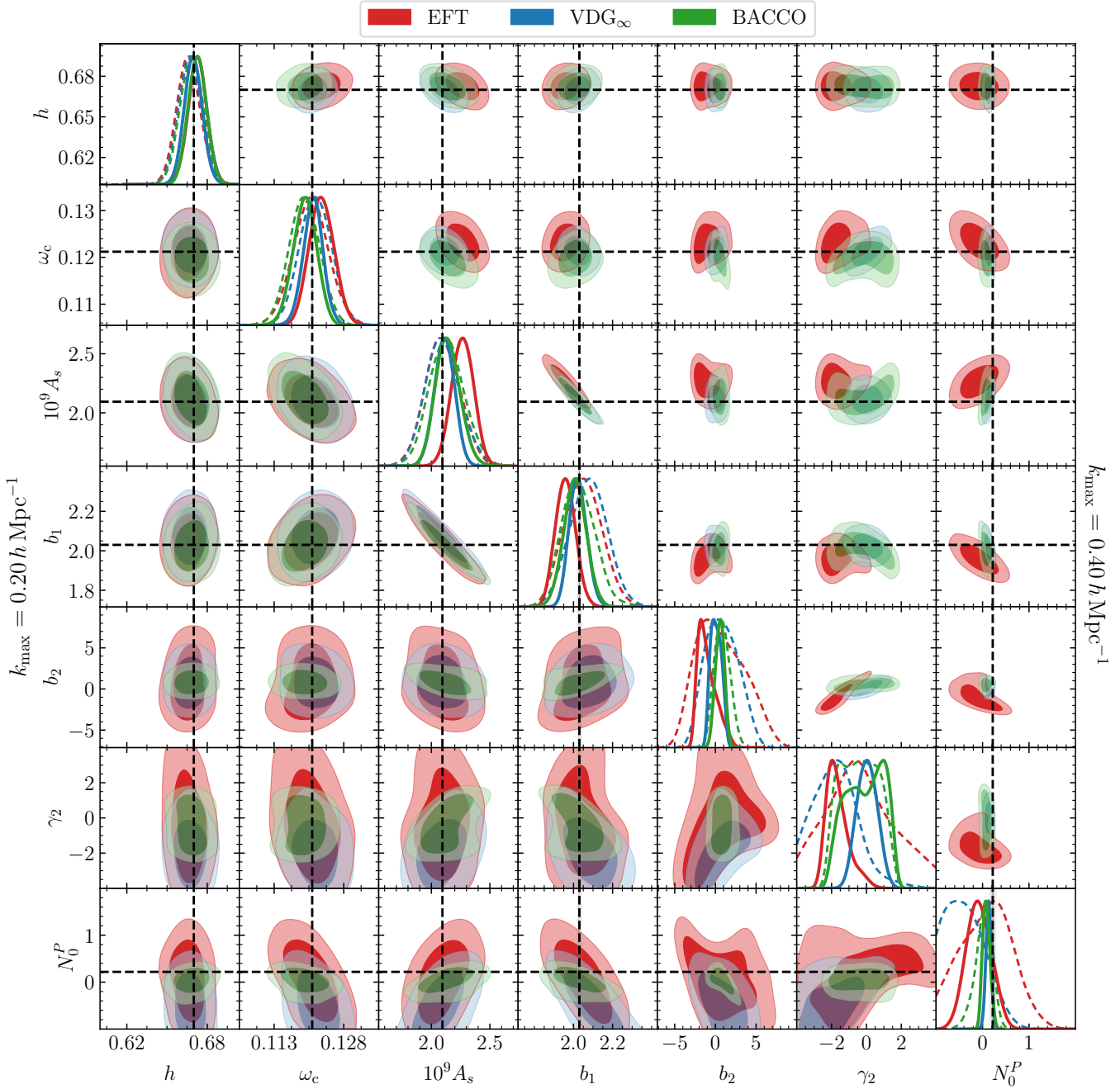


Fig. G.1. Triangular plots showing the marginalised posterior distributions of the cosmological parameters (h , ω_c , A_s), the linear bias b_1 , the second-order bias parameters (b_2 , γ_2), and the constant shot-noise parameter (N_0^P). Different colours correspond to different RSD models, as indicated in the legend. The panels correspond to the $z = 1.5$ snapshot. The *lower and upper triangles* show the configurations with $k_{\max} = 0.20 h \text{ Mpc}^{-1}$ and $k_{\max} = 0.40 h \text{ Mpc}^{-1}$, respectively. In the 1-dimensional contours, dashed and solid lines correspond to the two scale cuts. Dashed black lines for the cosmological parameters indicate their fiducial values. For b_1 and N_0^P , the dashed lines denote the best-fit parameters obtained from fitting only the large-scale limit of the $P_{\text{gg}}/P_{\text{mm}}$ ratio, as performed in previous works.